nature biotechnology

Article

https://doi.org/10.1038/s41587-026-03120-5

DNA-guided CRISPR–Cas12a effectors for programmable RNA recognition and cleavage

Received: 23 February 2026

Accepted: 1 April 2026

Published online: 01 May 2026

Check for updates

Xiaolong Wu[1,3], Wai Hei Lam[2,3], Zibin Zhao[1], Yumeng Cao[1], Haosi Lin[1], Xianzhen Feng[1], Yuanliang Zhai[2] & I-Ming Hsing[1]

CRISPR–Cas effectors typically rely on RNA guides to recognize target sequences. In Cas12a, the protospacer adjacent motif on DNA engages conserved protein residues, triggering target binding and nuclease activation. Here we reprogram Cas12a into a DNA-guided, RNA-targeting effector. Exploiting protospacer-adjacent motif-dependent interaction, we engineer synthetic CRISPR DNA that engages Cas12a to form a functional deoxyribonucleoprotein complex, while repurposing solely RNA as the programmable target. Structural, biophysical and biochemical analyses reveal the molecular basis of this DNA-guided, RNA-targeting configuration and support an activation pathway distinct from that of canonical RNA-guided systems. DNA-guided Cas12a enables direct RNA detection and efficient intracellular RNA knockdown, establishing a modular activation architecture for CRISPR–Cas12a and expanding the design space for programmable RNA manipulation.

Natural CRISPR–Cas adaptive immune systems are described widely as RNA-guided machineries that recognize and degrade invading mobile genetic elements[1,2]. In well-characterized Class 2 systems, including Type II Cas9 and Type V Cas12a, short CRISPR-derived RNAs provide sequence information for target recognition, whereas the Cas proteins execute nucleic acid cleavage[3,4]. The functional guide RNA is composed of a CRISPR RNA (crRNA) base-paired with a *trans*-activating crRNA (tracrRNA), which together form a structured RNA scaffold recognized by Cas9[4]. By contrast, Type V Cas12a requires only a single crRNA, in which the processed repeat-derived handle folds into a conserved pseudoknot structure that engages the Cas12a protein directly[3]. In these systems, the guide serves a dual role: encoding target sequence information and stabilizing a surveillance-competent Cas conformation[5,6]. Mechanistically, Cas proteins assemble with their guides into inactive binary complexes that become licensed for target interrogation only after recognition of a protospacer adjacent motif (PAM) within foreign DNA[7–9]. Structural and biochemical studies have shown that PAM engagement precedes extensive guide–target pairing and induces conserved conformational rearrangements that activate nuclease function[3,7,8,10]. These observations suggest that PAM recognition constitutes an initial checkpoint in CRISPR activation, independent of guide–target complementarity. Efforts to broaden targeting, through PAM engineering[11,12], RNA guides reprogramming[13,14] and protein mutagenesis[15,16], have improved flexibility, but have implicitly preserved the assumption that an RNA guide is a fundamental biochemical requirement for Cas activity. Bulk biochemical measurements indicate that Cas–guide RNA binary complexes can nonspecifically associate with PAM-rich DNA, revealing an intrinsic DNA-binding propensity often invoked to explain off-target effects[5,17–19]. Here we asked whether this strategy could be inverted, and RNA-guided effectors could be repurposed into DNA-guided, RNA-targeting platforms. We engineer synthetic CRISPR DNA (crDNA) that exploits PAM-dependent activation to assemble a functional deoxyribonucleoprotein (DNP) complex, and combine structural, biochemical and cellular analyses to define

[1]Department of Chemical and Biological Engineering, Hong Kong University of Science and Technology, Hong Kong, China. [2]Division of Life Science, Hong Kong University of Science and Technology, Hong Kong, China. [3]These authors contributed equally: Xiaolong Wu, Wai Hei Lam. e-mail: kehsing@ust.hk

the molecular basis of this alternative activation pathway. This work establishes a previously unrecognized mode of CRISPR activation and expands the design space for programmable RNA manipulation.

Programmable RNA recognition and cleavage with DNA-guided CRISPR–Cas12a

This reasoning prompted us to ask whether the informational role of the guide and the structural role of PAM engagement could be decoupled physically, such that PAM-mediated activation is provided by a DNA element while sequence specificity is supplied by an RNA substrate. Conformational studies of Cas12a *trans*-cleavage on heteroduplex substrates revealed that a 3′–5′ crDNA, bearing a stem–loop inverted relative to conventional crRNA, paired with its complementary RNA unexpectedly activates the *trans*-cleavage activity of Cas12a (Supplementary Fig. 1). To understand this phenomenon, we performed AlphaFold-guided modeling and molecular docking[20], which showed that crDNA occupies the canonical double-stranded DNA (dsDNA)-binding groove; its duplex region, including the PAM, interacts with the groove formed by the wedge (WED), recognition 1 (REC1) and PAM-interacting (PI) domains rather than the WED and endonuclease RuvC (homology domain of UV-sensitive gene product C activity for resolving Holliday junction) domains (regarded as canonical crRNA repeat-derived handle binding domain)[21,22] (Fig. 1a). We therefore hypothesized that a synthetic DNA molecule mimicking key features of PAM-containing dsDNA could form a DNP complex with Cas12a and redirect the effector toward RNA substrates. Guided by this structural framework, we redesigned and optimized the crDNA architecture, enabling efficient reprogramming of Cas12a into a DNA-guided, RNA-targeting effector (Supplementary Fig. 2).

We performed cleavage experiments in vitro using a 5′-carboxyfluorescein (5′-FAM) labeled RNA targets (Supplementary Table 1), confirming that DNA-guided Cas12a binds and cleaves target RNA specifically (Fig. 1b and Supplementary Fig. 3). Further experiments indicate that RNA recognition and binding by Cas–crDNA complexes is Mg^{2+}-independent, whereas cleavage strictly requires Mg^{2+} (Supplementary Fig. 4), consistent with metal-dependent catalysis by the RuvC domain. High-resolution cleavage site mapping shows that DNA-guided Cas12a cuts at two, five and six bases downstream of the spacer (Fig. 1c,d). Notably, the cleavage site of DNA-guided Cas12a is different in the RNA-guided system, as here the RNA targets occupy canonical crRNA binding region, suggesting possible resemblance to 3′ pre-crRNA cleavage feature[23–25]. Consistent with this model, targeted mutagenesis of Cas12a demonstrated that DNA-guided RNA cleavage depends on the same RuvC catalytic residues required for dsDNA cleavage in canonical RNA-guided Cas12a, whereas residues implicated in 5′ crRNA array processing are dispensable (Supplementary Fig. 5). Together, these results establish that DNA-guided Cas12a engages RNA substrates through a mechanistically distinct yet catalytically conserved pathway.

We next assessed whether DNA-guided Cas12a supports robust target-induced *trans*-cleavage using a fluorophore-quencher-labeled single-stranded DNA (ssDNA) reporter. Across eight distinct RNA targets, DNA-guided Cas12a exhibited strong and reproducible *trans*-cleavage activity (Fig. 1e and Supplementary Fig. 6), indicating that activation is not restricted to specific sequences. Comparable *trans*-cleavage was observed across several Cas12a orthologs guided by crDNA (Fig. 1f), supporting the generality of this DNA-guided strategy. Kinetic analysis using Michaelis–Menten modeling revealed that, at equivalent concentrations of activating nucleic acids, the maximal *trans*-cleavage rate of DNA-guided Cas12a is approximately twofold lower than that of the canonical RNA-guided system (Fig. 1g). This reduction probably reflects the absence of stabilizing interactions provided by the repeat-derived RNA pseudoknot. Nevertheless, sensitivity assays demonstrated that DNA-guided Cas12a enables direct detection of RNA targets at picomolar concentrations without preamplification (Supplementary Fig. 7), comparable to established RNA-guided Cas12a diagnostic platforms[26,27].

Collectively, these results demonstrate that Cas12a can be reprogrammed efficiently into a DNA-guided effector capable of sequence-specific RNA recognition and robust *cis*- and *trans*-cleavage activities.

Structural basis for DNA-guided reprogramming of CRISPR–Cas12a

Although these biochemical and biophysical assays establish PAM-dependent activation by crDNA, they do not by themselves distinguish whether Cas12a is engaged through the canonical PAM-recognition pathway or through an alternative, noncanonical nucleic-acid-mediated mechanism. To define the structural basis of DNA-guided CRISPR–Cas12a activity, we determined the cryogenic electron microscopy (cryo-EM) structure of a ternary complex comprising AsCas12a, a single-stranded crDNA guide and a complementary RNA target. To reduce preferred orientation during data processing, particle orientations were rebalanced, yielding a final map at overall 3.17 Å resolution (Fig. 2a). In the resulting map, 41 of the 43 nucleotides (nt) of the crDNA and the first 23 nt of the RNA target were well resolved and modeled, forming a 20-bp DNA–RNA heteroduplex stabilized within the AsCas12a binding channel (Fig. 2e). As expected, the PAM sequence embedded within the single-stranded crDNA adopts a stem–loop conformation and is recognized specifically by the PI domain of Cas12a (Fig. 2b–d). Notably, the WEDIII domain exhibits high flexibility, consistent with the absence of a repeat-derived RNA pseudoknot in the DNA-guided system. Overall, the architecture of the crDNA-guided Cas12a complex closely resembles that of the canonical 20-bp R-loop formed with crRNA-mediated DNA targeting (PDB 8SFO)[28] (Supplementary Fig. 8a,c). In particular, the positioning of the PAM and the key PI residues are nearly superimposable (Supplementary Fig. 8k,l), underscoring the capacity of Cas12a to accommodate a PAM-bearing ssDNA guide while preserving its canonical target-recognition framework.

Close inspection of the nuclease (Nuc) domain revealed an additional density adjacent to its surface basic patch. Given that the Nuc domain sequence and the crDNA are modeled almost entirely with only a single unresolvable nucleotide of crDNA at each terminus, we speculate that this extra density corresponds to the 3′-downstream sequence of the RNA target. Focused three-dimensional (3D) classification around the Cas12a opening captured several conformational states of this density, which appear to extend continuously from the 3′ end of the RNA target in the DNA–RNA heteroduplex (Fig. 2f and Supplementary Fig. 8). This observation suggests that the downstream RNA segment folds back toward the catalytic cleft formed between the RuvC and Nuc domains, positioning it for cleavage.

Together, these structural data establish that crDNA can direct formation of a catalytically competent Cas12a ternary complex and provide a mechanistic framework for understanding how PAM-dependent DNA engagement enables subsequent RNA recognition and cleavage in this DNA-guided system.

A PAM-dependent model for crDNA engagement by Cas12a

Cryo-EM analyses of the crDNA–RNA–Cas12a ternary complex revealed that, despite the absence of the canonical repeat-derived RNA pseudoknot, the PAM sequence of crDNA occupies the PI domain of Cas12a in a geometry indistinguishable from that observed in RNA-guided ternary complexes and is associated with conformational rearrangements consistent with catalytic activation. In contrast, electrophoretic mobility shift assay (EMSA) experiments showed that, in the absence of a structured RNA guide, direct binding of RNA to Cas12a is weak (Supplementary Fig. 10), suggesting that RNA alone is insufficient to initiate productive complex formation.

https://doi.org/10.1038/s41587-026-03120-5

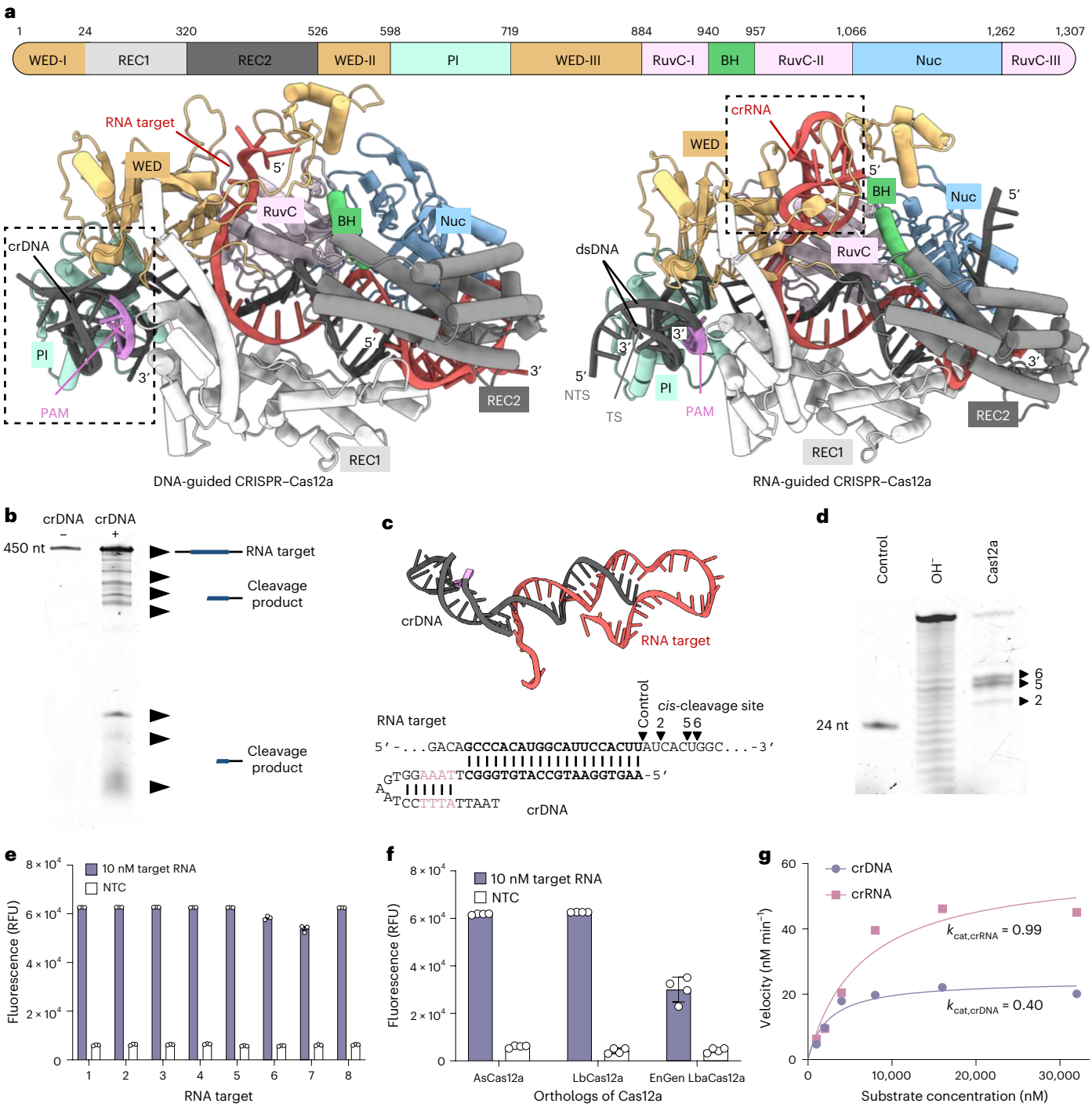


Fig. 1 | DNA-guided CRISPR–Cas12a cleaves ssRNA targets. a, Structural comparison of DNA-guided and RNA-guided CRISPR–Cas12a systems. Left: AlphaFold3-predicted model of a DNA-guided Cas12a ternary complex, in which the crDNA (black), containing a PAM sequence, basepairs with the target RNA (red). The resulting crDNA–RNA heteroduplex is positioned within a binding groove formed primarily by the WED (yellow), REC1 (light gray) and PI (mint green) domains. Right: structure of an RNA-guided Cas12a complex (PDB 5B43)[21], showing crRNA (red) engagement within the canonical RNA-binding channel. BH, bridge helix; NTS, nontarget strand; TS, target strand. **b**, Representative *cis*-cleavage assay of a 450-nt ssRNA target by Cas12a–crDNA. Representative gel image from three independent experiments with similar results. **c**, Sequence of the crDNA and its complementary ssRNA target, with the *cis*-cleavage site indicated. The PAM sequence is highlighted in pink. **d**, Mapping of Cas12a–crDNA *cis*-cleavage sites. Lanes labeled Control, OH^- and Cas12a indicate the 24-nt RNA control, alkaline hydrolysis ladder and Cas12a–crDNA cleavage products, respectively. Cleavage products corresponding to distinct sites are numbered. Representative gel image from three independent experiments with similar results. **e**, *Trans*-cleavage activity of DNA-guided Cas12a across eight different RNA targets: 10 nM target RNA, condition containing 10 nM input target RNA; NTC, no-target control. Bars: mean ± s.d.; $n = 3$ technical replicates. **f**, Comparison of DNA-guided Cas12a *trans*-cleavage activity across three Cas12a orthologs. Bars: mean ± s.d.; $n = 4$ technical replicates; 10 nM target RNA and NTC as in **e**. **g**, Kinetic analysis of *trans*-cleavage activity for DNA-guided and RNA-guided Cas12a systems. Datapoints are the mean of technical replicates. RFU, relative fluorescence units; $k_{cat,crRNA}$, apparent turnover number (min^{-1}) of Cas12a *trans*-cleavage activity when programmed with a CRISPR RNA (crRNA) guide; $k_{cat,crDNA}$, apparent turnover number (min^{-1}) of Cas12a *trans*-cleavage activity when programmed with a CRISPR DNA (crDNA) guide.

https://doi.org/10.1038/s41587-026-03120-5

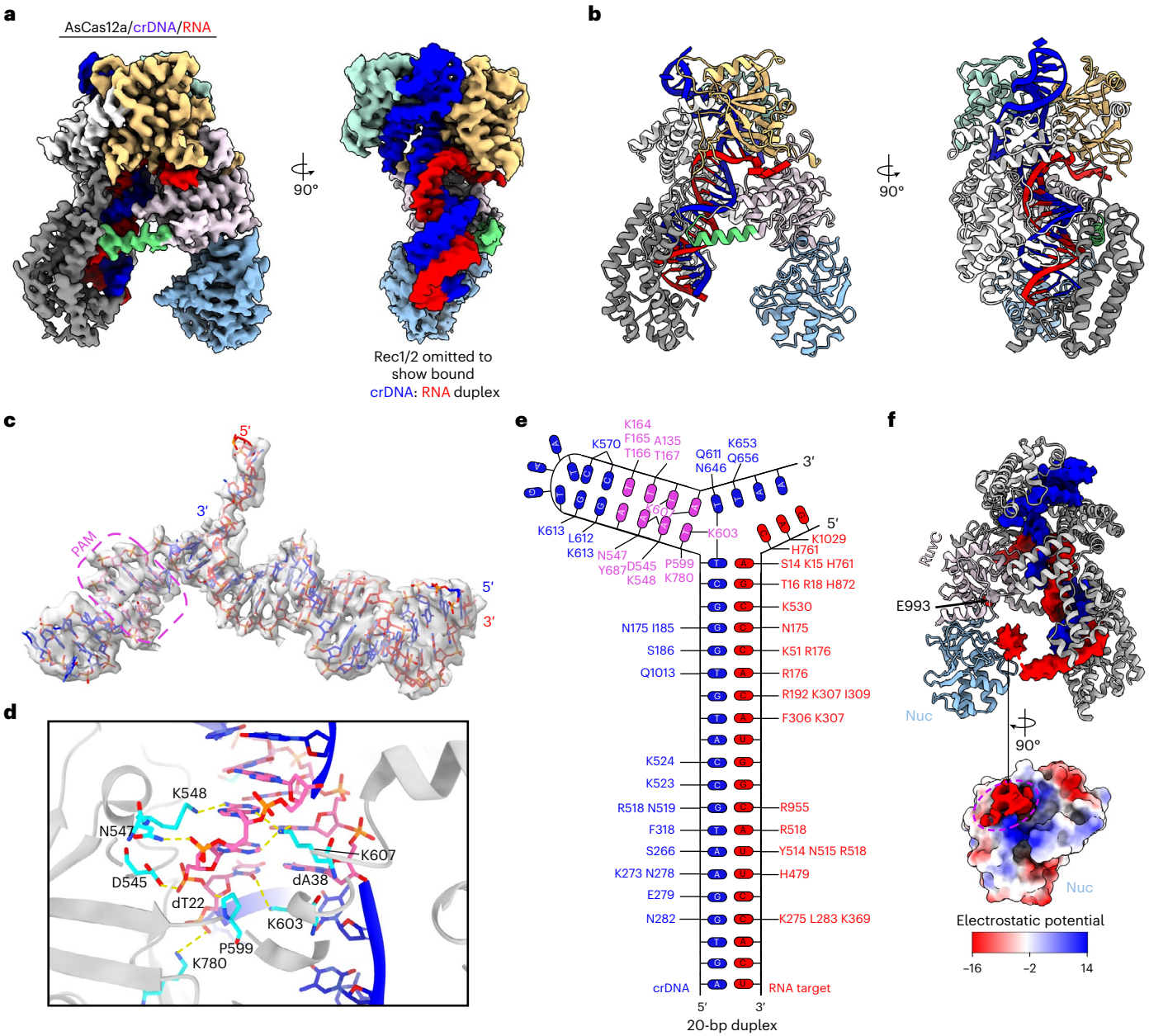


Fig. 2 | Structural basis for DNA-guided reprogramming of CRISPR–Cas12a. **a**, Left: top view of cryo-EM density of AsCas12a in complex with crDNA and target RNA. The density of AsCas12a is colored according to the scheme in Supplementary Fig. 9. Right: side view with densities of Rec1/2 domains omitted to show bound DNA–RNA duplex in the middle. **b**, Model of AsCas12a–crDNA–RNA fitted into the map in **a**. **c**, Density of crDNA (blue) and RNA (red) duplex. PAM sequence is highlighted in a pink box. **d**, Interaction between the PAM sequence of crDNA (pink) and AsCas12a. **e**, Schematic showing full protein–nucleic acid interactions between AsCas12a and visible DNA–RNA duplex. **f**, Top: an example class exhibiting extra density downstream of 3′ end of target RNA is observed at the opening of C-shaped AsCas12a and proximal to the nuclease site of AsCas12a, after focused 3D classification to resolve the heterogeneity. Important residue E993 at active site of AsCas12a nuclease domain is shown. Bottom: extra density of downstream RNA is found docking onto a basic patch of Nuc domain surface.

Based on these observations, we propose a model in which crDNA associates initially with apoCas12a to form a DNP complex through PAM-mediated interactions that subsequently recruits the complementary RNA target. In this framework, formation of the RNA–DNA duplex within the Cas12a binding channel induces further conformational rearrangements that activate both *cis*- and *trans*-cleavage activities. AlphaFold3 predictions support the feasibility of direct crDNA engagement by apoCas12a (Fig. 3a). Consistently, binary complex EMSA experiments, including competition assays with a fivefold excess of yeast RNA, demonstrate stable and specific binding between crDNA and apoCas12a, whereas random single-stranded DNA fails to form detectable complexes (Fig. 3b,c and Supplementary Fig. 11). Notably, the presence of yeast RNA increased modestly the fraction of unbound crDNA, suggesting that background RNA can compete partially with crDNA binding (Fig. 3c).

Limited trypsin proteolysis further revealed that crDNA binding induces a distinct conformational state of Cas12a, characterized by the appearance of a pronounced cleavage fragment at ~110 kDa and the disappearance of a fragment at ~130 kDa relative to apoCas12a (Fig. 3d). This pattern is indicative of an ordered conformational rearrangement rather than nonspecific association. Systematic mutation of the PAM sequence resulted in progressive increases in the dissociation

https://doi.org/10.1038/s41587-026-03120-5

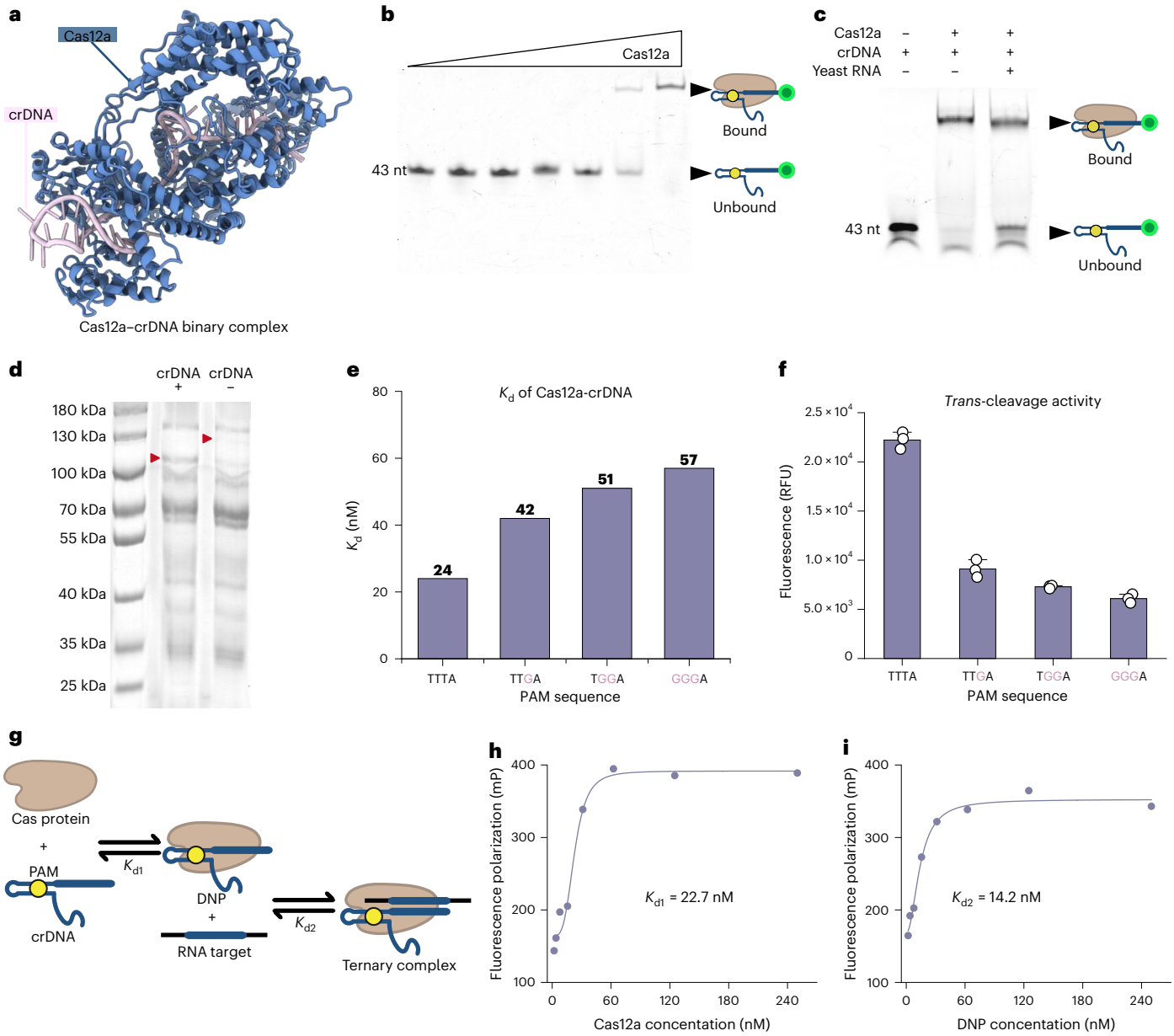


Fig. 3 | crDNA preferentially engages apoCas12a through PAM-dependent interactions. a, Model of the binary Cas12a–crDNA DNP complex, predicted by AlphaFold3. **b**, EMSA shows crDNA with PAM sequence binds with increased Cas12a. Representative EMSA image from three independent experiments with similar results. **c**, Cas12a–crDNA competing experiment with more than five times concentration of yeast RNA. **d**, Limited trypsin proteolysis suggests structural differences between apoCas12a and crDNA–Cas12a binary complex. Representative gel image from three independent experiments with similar results. **e**, Correlation between number of PAM mismatches and K_d increase. K_d was measured by fluorescence polarization assay. **f**, Correlation between number of PAM mismatches and *trans*-cleavage activity decrease; $n = 3$ technical replicates. Bars: mean ± s.d. **g**, Proposed model for DNA-guided Cas12a activation. **h**, Fluorescence polarization measurement for binary complex. **i**, Fluorescence polarization measurement for ternary complex. Datapoints are the mean of six independent experiments ($n = 6$), and the solid line represents a logistic fit to the average data.

constant (K_d) of the crDNA–Cas12a binary complex, accompanied by corresponding reductions in *trans*-cleavage activity (Fig. 3e,f and Supplementary Figs. 12 and 13). Complementary protein mutagenesis experiments further demonstrated that residues involved in PAM recognition are essential for maintaining efficient DNA-guided *trans*-cleavage activity (Supplementary Fig. 14).

Together, these data support a two-step binding and activation model for DNA-guided CRISPR–Cas12a (Fig. 3g). In this framework, Cas12a first associates with crDNA to form a PAM-dependent DNP complex characterized by dissociation constant K_{d1}, which subsequently binds the RNA target to generate the catalytically active ternary complex with dissociation constant K_{d2}. Fluorescence polarization measurements of K_{d1} and K_{d2} (Fig. 3h,i) revealed that binding affinities comparable in magnitude to those of canonical RNA-guided Cas12a systems (Supplementary Fig. 15). Notably, previously reported affinities for RNA-guided Cas12a span several orders of magnitude depending on the measurement approach[5,29,30]; when compared specifically with fluorescence polarization–based studies[31], the values obtained here fall within the same order of magnitude, underscoring the functional viability of this alternative activation pathway.

We also evaluated alternative binding scenarios, including initial association of apoCas12a with RNA or prehybridization of RNA with crDNA (Supplementary Fig. 16). Quantitative binding analyses showed that the affinity of apoCas12a for RNA is approximately an order of

magnitude weaker than that for crDNA, whereas the affinity between crDNA and RNA is comparable to that of the DNP complex. In practical applications, Cas12a and crDNA are supplied as reagents, whereas RNA represents the analyte or target. Under these conditions, the crDNA–apoCas12a engagement pathway predominates and is therefore the operationally relevant route in our system.

DNA-guided CRISPR–Cas system is RNA-specific targeting

Consistent with their established role as RNA-guided, DNA-targeting nucleases, RNA-guided Cas12a ribonucleoprotein (RNP) complexes readily bind single-stranded RNA (ssRNA), ssDNA and dsDNA (Fig. 4a and Supplementary Fig. 17), in agreement with previous reports of Watson–Crick-mediated target recognition[11,12,26]. By analogy, we initially anticipated that DNA-guided Cas12a, where crDNA bridges Cas12a and its RNA target through Watson–Crick base pairing, might similarly engage ssDNA substrates. EMSAs revealed that DNA-guided Cas12a binds exclusively to ssRNA, but not to either ssDNA or dsDNA (Supplementary Fig. 17). The absence of dsDNA binding is explained readily by pre-occupation of the PI groove by crDNA, which sterically precludes dsDNA engagement and unwinding. In contrast, the inability of DNA-guided Cas12a to bind ssDNA is striking, given the DNA-targeting ancestry of Cas12a. Fluorescence-based *trans*-cleavage assays corroborated these binding data: whereas RNA-guided Cas12a exhibits robust collateral cleavage activity against ssRNA, ssDNA and dsDNA, the DNA-guided system is selectively activated only by ssRNA (Fig. 4b and Supplementary Fig. 18). We propose that, in the DNA-guided complex, the canonical guide-binding channel of Cas12a preferentially accommodates RNA bases while disfavoring DNA, thereby enforcing RNA selectivity at the level of heteroduplex formation. In this model, crDNA–ssDNA hybrids fail to be retained stably within the binding channel and are displaced competitively, preventing productive complex assembly. Molecular simulations support this interpretation, demonstrating stable ternary complex formation between Cas12a, crDNA and RNA, whereas crDNA–ssDNA duplexes dissociate from Cas12a during equilibration (Supplementary Fig. 19).

To evaluate sequence requirements systematically, we tested eight orthogonal crDNA guides and their corresponding RNA targets. Both *cis*- and *trans*-cleavage activities were activated robustly only when the RNA target was fully complementary to the crDNA spacer (Fig. 4c,d and Supplementary Fig. 20), demonstrating stringent RNA-sequence dependence of DNA-guided Cas12a activation.

It is notable that the DNA-guided Cas12a system discriminates single-nucleotide mismatches in the spacer; compared with the fully complementary target (wild type (WT)), most point mutations significantly reduced *trans*-cleavage-induced fluorescence ($P < 0.05$; Fig. 4e,f and Supplementary Table 2), with the strongest effects observed at seed-region positions (the first, second and fourth nucleotides). Mutations at the 5th, 19th and 20th nucleotides did not significantly alter activity; mismatches at the 19th and 20th nucleotide even increased the fluorescence signal. Furthermore, truncating the spacer of crDNA from 20 nt to 16 nt increased the single-nucleotide specificity, especially at 12th and 15th nucleotides; signal was reduced by sevenfold and fivefold, respectively. Similar anomalous increases in collateral activity upon distal mismatches have been reported in RNA-targeting CRISPR systems[26,32], possibly reflecting altered steric interactions among *cis*-cleavage products, the nontarget strand overhang, and Cas12a[24,33]. Collectively, these findings establish that DNA-guided Cas12a can achieve improved single-nucleotide discrimination under optimized crDNA architectures while maintaining RNA selectivity, providing a foundation for the future development of sequence-specific RNA targeting and sensitive nucleic acid detection workflows.

Programmable nucleic acid diagnostic with DNA-guided CRISPR–Cas12a system

DNA-guided CRISPR–Cas systems provide a previously unexplored framework for molecular diagnostics by decoupling target recognition from RNA-guided surveillance[34–37]. To further enhance sensitivity and enable practical diagnostic applications, we developed Specific Locus Evaluation Utilizing Targeted Hydrolysis (SLEUTH)—an in vitro nucleic acid detection platform that integrates isothermal amplification with DNA-guided Cas12a-mediated *trans*-cleavage of a fluorescent reporter (Fig. 5a).

In SLEUTH, DNA or RNA targets are first amplified using recombinase polymerase amplification (RPA) or reverse transcription RPA (RT–RPA), respectively, followed by T7 transcription to generate RNA substrates. These RNA products subsequently activate DNA-guided Cas12a effectors, triggering robust *trans*-cleavage of a fluorogenic reporter and enabling real-time signal readout. This signal transduction architecture is conceptually analogous to SHERLOCK[38–40] but relies on a fundamentally distinct DNA-guided CRISPR effector system.

Using this workflow, SLEUTH achieved attomolar sensitivity (1 aM) for both RNA and DNA targets (Fig. 5b,c). When applied to clinical testing, SLEUTH accurately classified 31 SARS-CoV-2 patient samples (30 positive, 1 negative), showing 100% concordance with quantitative PCR with reverse transcription (RT–qPCR) results within this limited sample set (Fig. 5d,e and Supplementary Table 3). These results demonstrate that DNA-guided Cas12a retains diagnostic performance comparable to established RNA-guided platforms while operating within a distinct mechanistic framework.

Compared with SHERLOCK[38–40], SLEUTH is built on Cas12a and synthetic DNA guides, eliminating the need for engineered RNA components in the effector complex. Although amplification-based preprocessing remains essential for high-sensitivity detection, the exclusive use of DNA guides provides advantages in reagent stability, storage and manufacturing, which are relevant for large-scale production and deployment. These features highlight DNA-guided Cas12a as a complementary framework for CRISPR diagnostics, expanding the design space beyond conventional RNA-guided architectures.

Intracellular RNA knockdown with DNA-guided CRISPR–Cas system

Bacterial RNA interference is mediated naturally by RNA-guided CRISPR systems such as Cas13. Whether such a DNA-guided activation mechanism could operate within the complex intracellular environment, where crDNA stability, delivery efficiency and competition with endogenous nucleic acids may impose additional constraints, remains

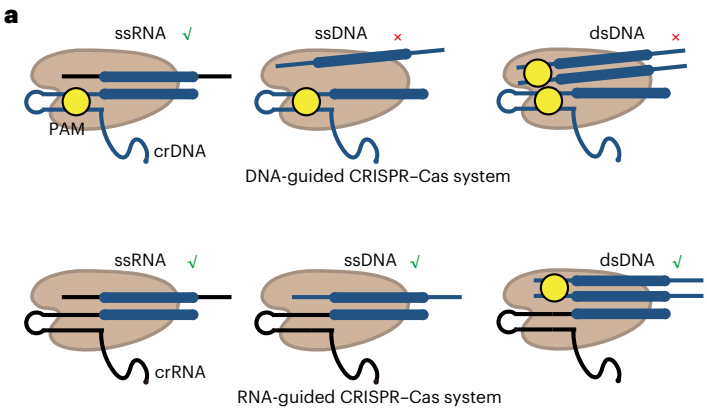
Fig. 4 | DNA-guided CRISPR–Cas system is RNA-specific targeting. a, Target-selectivity schematic of DNA-guided and RNA-guided CRISPR–Cas system. **b**, *Trans*-cleavage activity tests showing the target specificity of the DNA-guided Cas12a in comparison with the RNA-guided version of the same protein; $n = 3$ technical replicates. **c**, Orthogonal cleavage assay results of DNA-guided Cas12a *cis*-cleavage activity across eight crDNA–RNA pairs. Representative gel image from three independent experiments with similar results. **d**, Orthogonal heat map of DNA-guided Cas12a *trans*-cleavage activity across eight crDNA–RNA pairs. Each cell represents the mean fluorescence signal from three technical replicates ($n = 3$), with color intensity indicating average *trans*-cleavage activity. **e**, Schematic of single-nucleotide specificity test sequence. **f**, Single-nucleotide specificity of DNA-guided CRISPR–Cas12a system with 20-nt spacer; $n = 3$ technical replicates. Statistical significance was assessed by ordinary one-way analysis of variance (ANOVA) followed by Dunnett's multiple comparisons test (each group compared with the NTC group; two-sided). **g**, Single-nucleotide specificity of DNA-guided CRISPR–Cas12a system with 16-nt spacer; $n = 3$ technical replicates. Statistical significance was assessed by ordinary one-way ANOVA followed by Dunnett's multiple comparisons test (each group compared with the NTC group; two-sided). Exact *P* values are provided in Supplementary Table 2; bars: mean ± s.d.

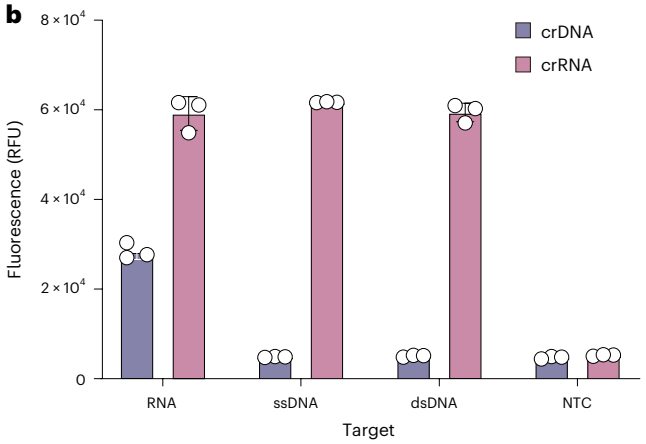
https://doi.org/10.1038/s41587-026-03120-5

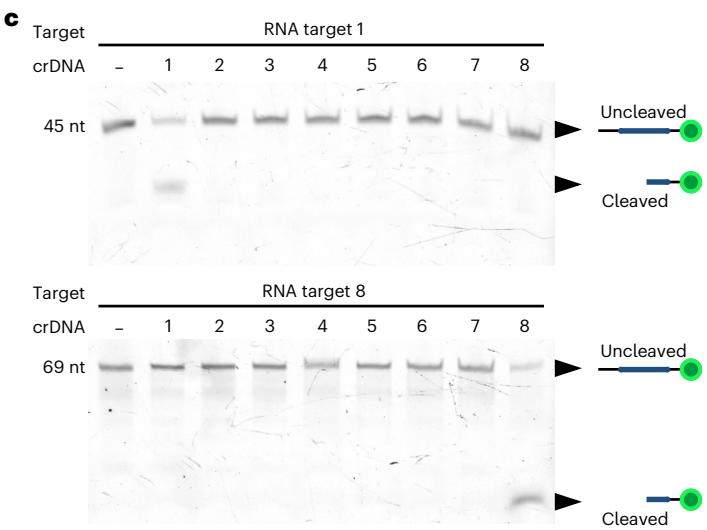
unclear. Here we examined whether a DNA-guided CRISPR–Cas12a system is capable of mediating sequence-specific RNA knockdown in mammalian cells.

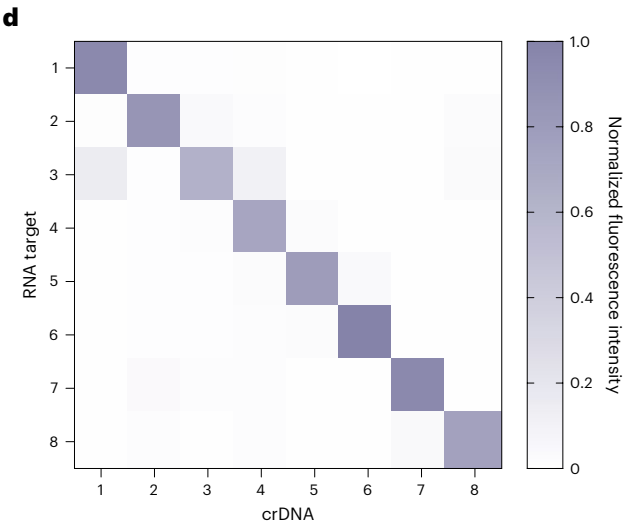
To this end, we established an enhanced green fluorescent protein (EGFP)-based cellular RNA knockdown assay in HEK293T cells (Fig. 6a). Cas12a was coexpressed with mCherry from a single plasmid to enable monitoring of Cas12a expression, whereas the EGFP transgene was encoded on a separate plasmid as a reporter. Targeting crDNAs were labeled fluorescently with Cy5 to assess intracellular delivery.

Cells were cotransfected with the Cas12a expression plasmid, the EGFP reporter plasmid and crDNAs, followed by a 12-h incubation. EGFP fluorescence was evaluated by fluorescence microscopy and flow cytometry, and EGFP mRNA levels were quantified by RT–qPCR. Given previous evidence that phosphorothioate (PS) modifications enhance

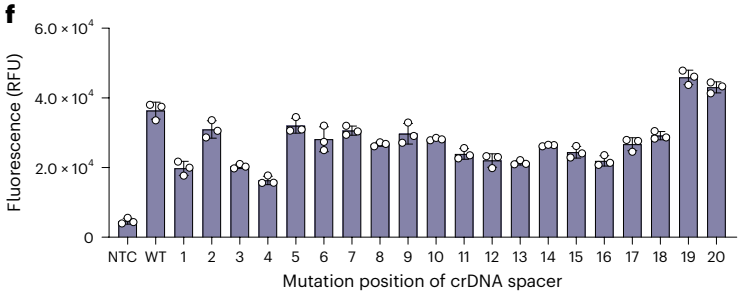


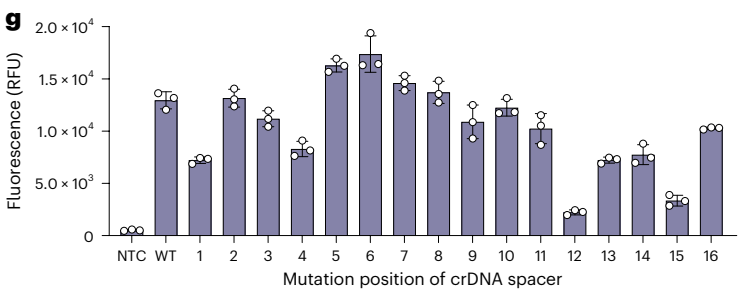












https://doi.org/10.1038/s41587-026-03120-5

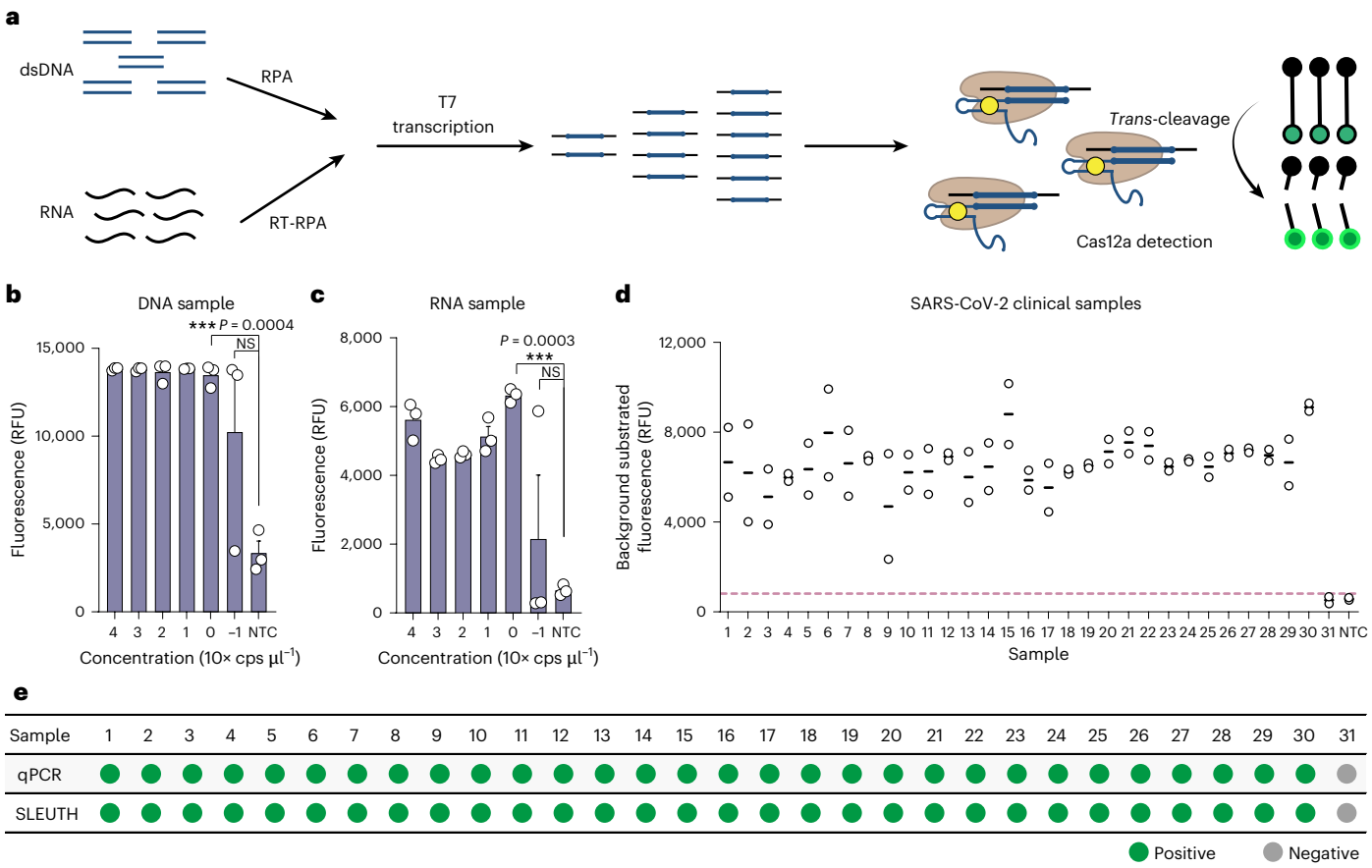


Fig. 5 | Programmable nucleic acid diagnostic with DNA-guided CRISPR–Cas12a system. a, Workflow for SLEUTH assay. **b**, DNA mimic sample sensitivity test with SLEUTH; $n = 3$ technical replicates. Statistical significance was assessed by ordinary one-way ANOVA followed by Dunnett's multiple comparisons test (each group compared with the NTC group; two-sided). $^{*}P < 0.05$, $^{**}P < 0.01$, $^{***}P < 0.001$, NS: nonsignificant; bars: mean ± s.d. **c**, RNA mimic sample sensitivity test with SLEUTH; $n = 3$ technical replicates. Statistical significance was assessed by ordinary one-way ANOVA followed by Dunnett's multiple comparisons test (each group compared with the NTC group; two-sided). $^{*}P < 0.05$, $^{**}P < 0.01$, $^{***}P < 0.001$; bars: mean ± s.d. **d**, SARS-CoV-2 clinical samples detection with SLEUTH; $n = 2$ technical replicates per sample. Threshold is defined as the limit of blank plus three times the s.d. **e**, Detection results by qPCR and SLEUTH, respectively ($n = 31$ clinical samples).

intracellular stability and target engagement of oligonucleotides, we compared an unmodified crDNA with a chemically stabilized crDNA containing four PS linkages at both the 5′ and 3′ termini (Fig. 6b).

Cotransfection of Cas12a with EGFP-targeting, PS-modified crDNA resulted in a pronounced reduction in EGFP fluorescence (Fig. 6c and Supplementary Fig. 21). Flow cytometry analysis revealed an approximately 56% decrease in EGFP mean fluorescence intensity (MFI) relative to nontargeting crDNA controls, whereas no appreciable reduction was observed with the unmodified crDNA (Fig. 6d). Consistently, RT–qPCR analysis showed a corresponding decrease in EGFP mRNA levels (76%) upon treatment with PS-modified crDNA–Cas12a complexes (Fig. 6e). Transfection of crDNA alone, in the absence of Cas12a, did not affect EGFP expression, indicating that RNA knockdown is Cas12a-dependent (Fig. 6f,g and Supplementary Fig. 22). RT–qPCR analysis of nontarget transcripts encoded by the macrophage migration inhibitory factor (*MIF*) and beta-2-microglobulin (*B2M*) genes showed no detectable changes, indicating sequence specificity (Fig. 6h). Transcriptome-wide RNA sequencing further confirmed minimal off-target effects (Supplementary Fig. 23). To extend beyond a reporter system, we next examined an endogenous transcript encoded by the *MIF* gene. RT–qPCR revealed sequence-dependent knockdown of *MIF* mRNA mediated by DNA-guided Cas12a (Supplementary Fig. 24).

Together, these results demonstrate that DNA-guided CRISPR–Cas12a can mediate sequence-specific RNA cleavage in mammalian cells, providing a cellular framework for subsequent evaluation of this system in intracellular RNA virus inhibition models.

Discussion

This study demonstrates that RNA targeting by CRISPR–Cas effectors does not depend intrinsically on RNA-guided activation. Instead, Cas12a can be functionally reconfigured into a DNA-guided, RNA-targeting system in which structural activation and sequence recognition are decoupled. This finding challenges the prevailing assumption, implicit in both natural CRISPR biology and most engineering efforts, that an RNA guide is a biochemical requirement for Cas activation. Previous efforts to expand the specificity and versatility of CRISPR systems have operated largely within the canonical RNA-guided framework, focusing on relaxing or engineering PAM constraints, chemical modification of guide RNAs, construction of DNA–RNA chimeric guides or protein engineering to enable RNA recognition by DNA-targeting effectors[41–44]. In contrast to these approaches, our work exploits PAM recognition itself as a design principle to reconfigure the CRISPR–Cas12a activation pathway, decoupling guide-mediated activation from RNA-based target recognition. This architecture enables DNA to serve as the guiding scaffold while RNA is repurposed exclusively as the programmable target—a configuration not observed in known natural CRISPR systems.

By integrating cryo-EM structural analysis, artificial intelligence (AI)-assisted modeling and quantitative biophysical measurements, we delineate the molecular basis of DNA-guided Cas12a activation

https://doi.org/10.1038/s41587-026-03120-5

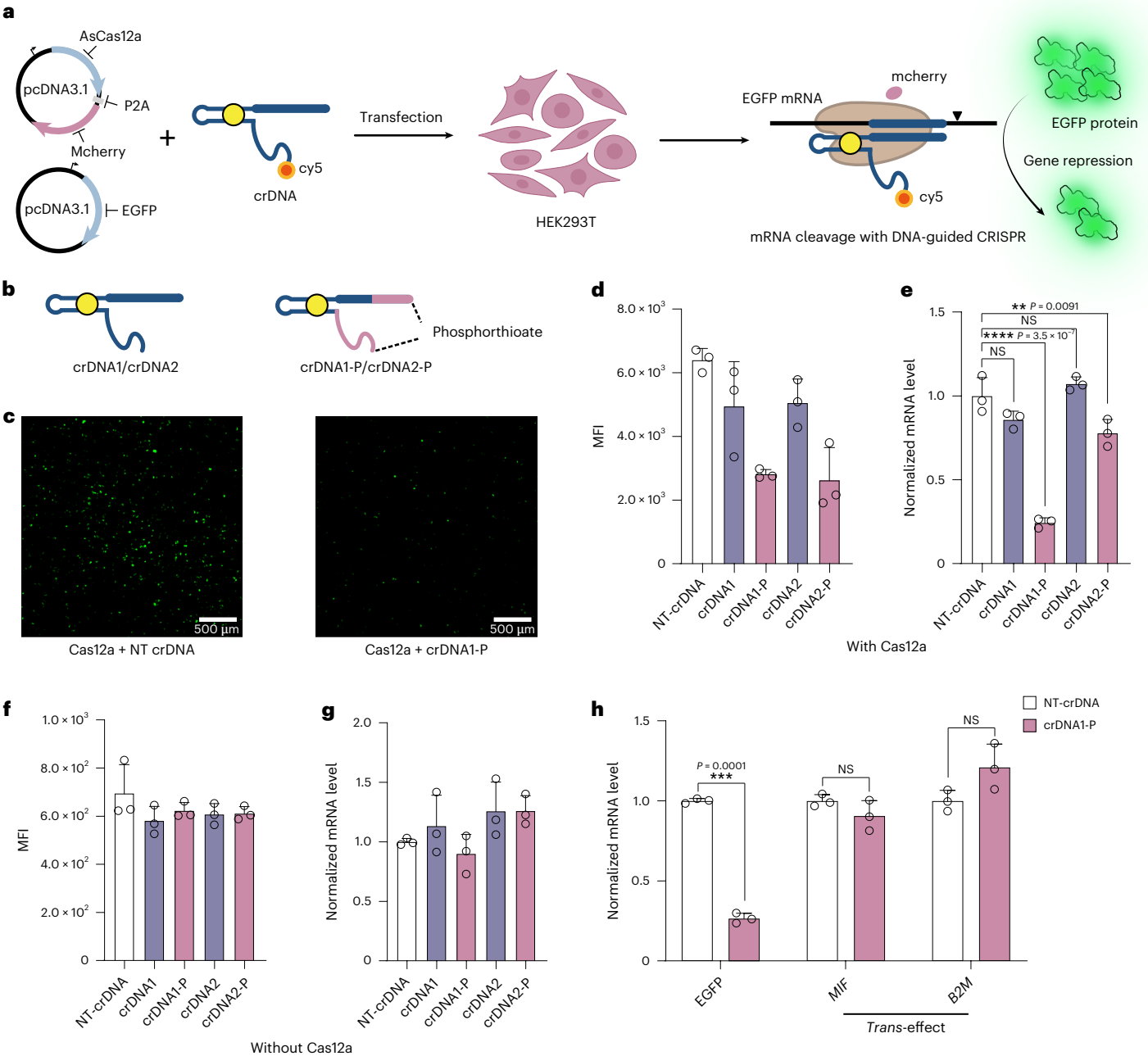


Fig. 6 | Intracellular RNA knockdown with DNA-guided CRISPR–Cas system. **a**, Schematics of EGFP RNA knockdown with DNA-guided CRISPR–Cas system in HEK293T cells. **b**, Schematic of PS modification of crDNA. The crDNA contains PS linkages at the first four and last four nucleotides. PS-modified positions are highlighted in pink. **c**, Representative fluorescence images showing EGFP expression in cells transfected with nontargeting crDNA (left) or EGFP-targeting crDNA (right). Representative image from three independent experiments with similar results. **d**, Geometric MFI of EGFP in cells treated with different crDNA–Cas12a complexes. MFI values were calculated exclusively from mCherry–Cy5–positive cells; $n = 3$ technical replicates. Bars: mean ± s.d. **e**, Normalized EGFP mRNA levels following treatment with different crDNA–Cas12a complexes, quantified by RT–qPCR and normalized to the transcript encoded by the *GAPDH* gene; $n = 3$ biological replicates; each with three technical replicates. Statistical significance was assessed by ordinary one-way ANOVA followed by Dunnett's multiple comparisons test (each group compared with the NT-crDNA group; two-sided). $^{*}P < 0.05$, $^{**}P < 0.01$, $^{***}P < 0.001$, $^{****}P < 0.0001$; bars: mean ± s.d. **f**, Geometric MFI of EGFP in cells treated with different crDNA. MFI values were calculated exclusively from mCherry–Cy5–positive cells; $n = 3$ technical replicates. Bars: mean ± s.d. **g**, Normalized EGFP mRNA expression levels following treatment with different crDNA, quantified by RT–qPCR and normalized to *GAPDH* mRNA; $n = 3$ biological replicates, each with three technical replicates. Bars: mean ± s.d. **h**, Specificity test with nontarget mRNA (*MIF* and *B2M*) by RT–qPCR and normalized to the *GAPDH* mRNA; $n = 3$ technical replicates. Statistical significance was assessed by ordinary one-way ANOVA followed by Dunnett's posttest (two-sided). $^{*}P < 0.05$, $^{**}P < 0.01$, $^{***}P < 0.001$; bars: mean ± s.d.

and RNA targeting. Our data demonstrate that this unconventional configuration supports high RNA specificity and robust activity in both molecular diagnostics and cellular RNA knockdown. Together, these results expand the functional design space of CRISPR-based RNA manipulation and establish a mechanistic framework for engineering DNA-guided CRISPR effectors.

More broadly, our findings suggest that the catalytic scope of type V CRISPR nucleases may be more flexible than generally

appreciated[45]. In our system, mutation of the canonical RuvC catalytic residue abolished both *cis*-RNA cleavage and *trans*-ssDNA cleavage, consistent with a RuvC-dependent mechanism for RNA cleavage in the DNA-guided Cas12a configuration. This interpretation is in line with growing evidence that RuvC domains in some Cas12 effectors can accommodate RNA substrates in specific mechanistic contexts[12,26,46,47]. Notably, recent work on Cas12a3 (ref. 48) showed that, after target RNA recognition, the effector loads tRNA substrates into its RuvC domain for cleavage of the 3′CCA tail, providing a naturally occurring example of RuvC-mediated RNA cleavage within the Cas12a family. Our results therefore extend this emerging view by showing that programmable RNA cleavage can also be achieved in a DNA-guided Cas12a framework.

RNA-guided, RNA-targeting systems such as Cas13 have proven powerful for molecular diagnostics and transcript regulation but are associated frequently with indiscriminate collateral cleavage and, in cellular contexts, measurable toxicity[37,38,49–52]. In contrast, in cellular contexts, Cas12a has been reported to display more limited collateral *trans*-cleavage, which may provide a more controllable starting point for RNA-targeting applications[53]. Although DNA-guided Cas12a currently mediates only modest knockdown of endogenous transcripts, and thus at present represents a proof of concept rather than a fully optimized platform, these findings establish the feasibility of programmable RNA targeting by a DNA-guided CRISPR effector. With further optimization, DNA-guided Cas12a and related effectors may be developed into versatile tools for RNA knockdown, antiviral intervention and live-cell RNA imaging. Extending the DNA-guiding concept to other compact CRISPR effectors, such as Cas12j (CasΦ) or Cas12f (Cas14), may further facilitate delivery and broaden therapeutic applicability[54,55].

Beyond applications, our findings prompt reconsideration of the canonical assembly pathway of CRISPR effectors. The prevailing model posits that Cas proteins first assemble into RNP complexes before target engagement[3,4]. In contrast, our data support an alternative pathway in which Cas12a can initially associate with PAM-containing DNA to form a DNP complex that subsequently recruits its RNA substrate. Currently demonstrated for Cas12a, this model raises broader questions regarding the thermodynamic and kinetic landscape of CRISPR target recognition and suggests the existence of previously unappreciated Cas–DNA intermediates. The cellular behavior and biological consequences of such intermediates remain important subjects for future investigation.

Finally, several limitations and opportunities for optimization remain. The DNP complex exhibits lower stability than the canonical RNP, probably reflecting intrinsic differences in nucleic acid recognition and binding energetics. Directed evolution strategies, potentially guided by AI, may enable concurrent optimization of DNA guide architecture and Cas variants to enhance DNP stability and activity. In addition, we observed progressive guide self-cleavage that inactivates both RNA- and DNA-guided systems over time, even under magnesium-free storage conditions (Supplementary Fig. 25). Chemical stabilization strategies, such as PS backbone modification, may therefore be essential for extending effector lifetime and performance in both research and therapeutic contexts.

Online content

Any methods, additional references, Nature Portfolio reporting summaries, source data, extended data, supplementary information, acknowledgements, peer review information; details of author contributions and competing interests; and statements of data and code availability are available at https://doi.org/10.1038/s41587-026-03120-5.

References

1. Wang, J. Y. & Doudna, J. A. CRISPR technology: a decade of genome editing is only the beginning. *Science* **379**, eadd8643 (2023).
2. Pacesa, M., Pelea, O. & Jinek, M. Past, present, and future of CRISPR genome editing technologies. *Cell* **187**, 1076–1100 (2024).
3. Zetsche, B. et al. Cpf1 is a single RNA-guided endonuclease of a class 2 CRISPR–Cas system. *Cell* **163**, 759–771 (2015).
4. Jinek, M. et al. A programmable dual-RNA-guided DNA endonuclease in adaptive bacterial immunity. *Science* **337**, 816–821 (2012).
5. Sternberg, S. H., Redding, S., Jinek, M., Greene, E. C. & Doudna, J. A. DNA interrogation by the CRISPR RNA-guided endonuclease Cas9. *Nature* **507**, 62–67 (2014).
6. Cofsky, J. C., Soczek, K. M., Knott, G. J., Nogales, E. & Doudna, J. A. CRISPR-Cas9 bends and twists DNA to read its sequence. *Nat. Struct. Mol. Biol.* **29**, 395–402 (2022).
7. Yamano, T. et al. Structural basis for the canonical and non-canonical PAM recognition by CRISPR-Cpf1. *Mol. Cell* **67**, 633–645 (2017).
8. Anders, C., Niewoehner, O., Duerst, A. & Jinek, M. Structural basis of PAM-dependent target DNA recognition by the Cas9 endonuclease. *Nature* **513**, 569–573 (2014).
9. Jiang, F. G. et al. Structures of a CRISPR–Cas9 R-loop complex primed for DNA cleavage. *Science* **351**, 867–871 (2016).
10. Knight, S. C. et al. Dynamics of CRISPR–Cas9 genome interrogation in living cells. *Science* **350**, 823–826 (2015).
11. O'Connell, M. R. et al. Programmable RNA recognition and cleavage by CRISPR/Cas9. *Nature* **516**, 263–266 (2014).
12. Rananaware, S. R. et al. Programmable RNA detection with CRISPR–Cas12a. *Nat. Commun.* **14**, 5409 (2023).
13. Jiao, C. L. et al. Noncanonical crRNAs derived from host transcripts enable multiplexable RNA detection by Cas9. *Science* **372**, 941–948 (2021).
14. Jiao, C. L. et al. TracrRNA reprogramming enables direct PAM-independent detection of RNA with diverse DNA-targeting Cas12 nucleases. *Nat. Commun.* **15**, 5909 (2024).
15. Silverstein, R. A. et al. Custom CRISPR–Cas9 PAM variants via scalable engineering and machine learning. *Nature* **643**, 539–550 (2025).
16. Shi, Y. J. et al. DNA topology regulates PAM–Cas9 interaction and DNA unwinding to enable near-PAMless cleavage by thermophilic Cas9. *Mol. Cell* **82**, 4160–4175 (2022).
17. Degtev, D. et al. Engineered PsCas9 enables therapeutic genome editing in mouse liver with lipid nanoparticles. *Nat. Commun.* **15**, 9173 (2024).
18. Shi, H. L. et al. Rapid two-step target capture ensures efficient CRISPR–Cas9-guided genome editing. *Biophys. J.* **124**, 1730–1742 (2025).
19. Bhattacharya, S., Agarwal, A. & Muniyappa, K. Deciphering the substrate specificity reveals that CRISPR-Cas12a is a bifunctional enzyme with both endo- and exonuclease activities. *J. Mol. Biol.* **436**, 168550 (2024).
20. Abramson, J. et al. Accurate structure prediction of biomolecular interactions with AlphaFold 3. *Nature* **630**, 493–500 (2024).
21. Yamano, T. et al. Crystal structure of Cpf1 in complex with guide RNA and target DNA. *Cell* **165**, 949–962 (2016).
22. Stella, S. et al. Conformational activation promotes CRISPR–Cas12a catalysis and resetting of the endonuclease activity. *Cell* **175**, 1856–1871 (2018).
23. Chen, J. et al. DNA target binding-induced pre-crRNA processing in type II and V CRISPR–Cas systems. *Nucleic Acids Res.* **53**, gkae1241 (2024).
24. Swarts, D. C., van der Oost, J. & Jinek, M. Structural basis for guide RNA processing and seed-dependent DNA targeting by CRISPR–Cas12a. *Mol. Cell* **66**, 221–233 (2017).
25. Fonfara, I., Richter, H., Bratovic, M., Le Rhun, A. & Charpentier, E. The CRISPR-associated DNA-cleaving enzyme Cpf1 also processes precursor CRISPR RNA. *Nature* **532**, 517–521 (2016).
26. Zhang, J. Y. et al. Intrinsic RNA targeting triggers indiscriminate DNase activity of CRISPR–Cas12a. *Angew. Chem. Int. Ed. Engl.* **63**, e202403123 (2024).

27. Nalefski, E. A. et al. Kinetic analysis of Cas12a and Cas13a RNA-guided nucleases for development of improved CRISPR-based diagnostics. *Iscience* **24**, 102996 (2021).
28. Strohkendl, I. et al. Cas12a domain flexibility guides R-loop formation and forces RuvC resetting. *Mol. Cell* **84**, 2717–2731 (2024).
29. Strohkendl, I., Saifuddin, F. A., Rybarski, J. R., Finkelstein, I. J. & Russell, R. Kinetic basis for DNA target specificity of CRISPR-Cas12a. *Mol. Cell* **71**, 816–824 (2018).
30. Singh, D. et al. Real-time observation of DNA target interrogation and product release by the RNA-guided endonuclease CRISPR Cpf1 (Cas12a). *Proc. Natl Acad. Sci. USA* **115**, 5444–5449 (2018).
31. Maji, B. et al. A high-throughput platform to identify small-molecule inhibitors of CRISPR–Cas9. *Cell* **177**, 1067–1079 (2019).
32. Tambe, A., East-Seletsky, A., Knott, G. J., Doudna, J. A. & O'Connell, M. R. RNA binding and HEPN-nuclease activation are decoupled in CRISPR–Cas13a. *Cell Rep.* **24**, 1025–1036 (2018).
33. Zhang, L. Y. et al. Systematic in vitro profiling of off-target affinity, cleavage and efficiency for CRISPR enzymes. *Nucleic Acids Res.* **48**, 5037–5053 (2020).
34. Cao, Y. M. et al. Benchtop to at-home test: amplicon-depleted CRISPR-regulated loop mediated amplification at skin-temperature for viral load monitoring. *Biosens. Bioelectron.* **267**, 116866 (2025).
35. Cao, Y. et al. CoLAMP: CRISPR-based one-pot loop-mediated isothermal amplification enables at-home diagnosis of SARS-CoV-2 RNA with nearly eliminated contamination utilizing amplicons depletion strategy. *Biosens. Bioelectron.* **236**, 115402 (2023).
36. Wu, X. et al. RatioCRISPR: a ratiometric biochip based on CRISPR/Cas12a for automated and multiplexed detection of heteroplasmic SNPs in mitochondrial DNA. *Biosens. Bioelectron.* **241**, 115676 (2023).
37. Wu, X. L. et al. LbuCas13a directly targets DNA and elicits strong trans-cleavage activity. *Nat. Biomed. Eng.* **9**, 2141–2154 (2025).
38. Gootenberg, J. S. et al. Nucleic acid detection with CRISPR-Cas13a/C2c2. *Science* **356**, 438–442 (2017).
39. Gootenberg, J. S. et al. Multiplexed and portable nucleic acid detection platform with Cas13, Cas12a and Csm6. *Science* **360**, 439–444 (2018).
40. Joung, J. et al. Detection of SARS-CoV-2 with SHERLOCK one-pot testing. *N. Engl. J. Med.* **383**, 1492–1494 (2020).
41. Hu, J. H. et al. Evolved Cas9 variants with broad PAM compatibility and high DNA specificity. *Nature* **556**, 57–63 (2018).
42. Nishimasu, H. et al. Engineered CRISPR–Cas9 nuclease with expanded targeting space. *Science* **361**, 1259–1262 (2018).
43. Walton, R. T., Christie, K. A., Whittaker, M. N. & Kleinstiver, B. P. Unconstrained genome targeting with near-PAMless engineered CRISPR–Cas9 variants. *Science* **368**, 290–296 (2020).
44. Donohoue, P. D. et al. Conformational control of Cas9 by CRISPR hybrid RNA–DNA guides mitigates off-target activity in T cells. *Mol. Cell* **81**, 3637–3649 (2021).
45. Orosco, C. et al. DNA-guided CRISPR–Cas12 for cellular RNA targeting. *MedRxiv* https://doi.org/10.1101/2024.11.21.24317744 (2024).
46. Yan, W. X. et al. Functionally diverse type V CRISPR–Cas systems. *Science* **363**, 88–91 (2019).
47. Bravo, J. P. K. et al. RNA targeting unleashes indiscriminate nuclease activity of CRISPR–Cas12a2. *Nature* **613**, 582–587 (2023).
48. Dmytrenko, O. et al. RNA-triggered Cas12a3 cleaves tRNA tails to execute bacterial immunity. *Nature* **649**, 1312–1321 (2026).
49. Wei, J. Y. et al. Deep learning and CRISPR-Cas13d ortholog discovery for optimized RNA targeting. *Cell Syst.* **14**, 1087–1102 (2023).
50. Abudayyeh, O. O. et al. RNA targeting with CRISPR-Cas13. *Nature* **550**, 280–284 (2017).
51. Cox, D. B. T. et al. RNA editing with CRISPR-Cas13. *Science* **358**, 1019–1027 (2017).
52. Hart, S. K. et al. Precise RNA targeting with CRISPR–Cas13d. *Nat. Biotechnol.* **44**, 64–69 (2025).
53. Nguyen, G. T. et al. CRISPR–Cas12a exhibits metal-dependent specificity switching. *Nucleic Acids Res.* **52**, 9343–9359 (2024).
54. Harrington, L. B. et al. Programmed DNA destruction by miniature CRISPR–Cas14 enzymes. *Science* **362**, 839–842 (2018).
55. Pausch, P. et al. CRISPR-CasΦ from huge phages is a hypercompact genome editor. *Science* **369**, 333–337 (2020).

Publisher's note Springer Nature remains neutral with regard to jurisdictional claims in published maps and institutional affiliations.

Open Access This article is licensed under a Creative Commons Attribution 4.0 International License, which permits use, sharing, adaptation, distribution and reproduction in any medium or format, as long as you give appropriate credit to the original author(s) and the source, provide a link to the Creative Commons licence, and indicate if changes were made. The images or other third party material in this article are included in the article's Creative Commons licence, unless indicated otherwise in a credit line to the material. If material is not included in the article's Creative Commons licence and your intended use is not permitted by statutory regulation or exceeds the permitted use, you will need to obtain permission directly from the copyright holder. To view a copy of this licence, visit http://creativecommons.org/licenses/by/4.0/.

© The Author(s) 2026, modified publication 2026

Methods

Materials

Acidaminococcus sp. Cas12a (AsCas12a) and *Lachnospiraceae* bacterium Cas12a (LbCas12a) were from Tolo Biotech. AsCas12a Ultra was from Integrated DNA Technologies, Inc. EnGen LbaCas12a and NEbuffer r2.1 were from New England Biolabs. The RNA sequences and ssDNA sequences (Supplementary Table 1) were from GENEWIZ. HEPES buffer, magnesium chloride, Lipofectamine 3000 and UltraPure diethyl pyrocarbonate (DEPC)-treated H_2O were from Thermo Fisher Scientific. TwistAmp basic kit was from TwistDx. DNA amplification powder kit and RNA-amplification powder kit were from Amp-future. Ribonucleotide solution mix, deoxynucleotide solution mix, RNase inhibitor and T7 RNA polymerase were from New England Biolabs. TIANamp Virus DNA/RNA Kit was from Tiangen. PCR amplification premix kit was from Takara, MolPure Flash Cell/Tissue Total RNA Kit and RT–qPCR mix Hifair Advanced One Step RT–qPCR SYBR Green Kit were from Yeasen Biotechnology. RNA sequencing was performed by GENEWIZ. BeyoBlue Plus Coomassie Blue Super-Fast Staining Solution was from Beyotime. HEK293T (IM-H222) cells were from Xiamen Immocell Biotechnology Co., Ltd.

RNA cleavage assays

Unless otherwise stated, cleavage reactions contained 5′-FAM-labeled target RNA or label-free target RNA (100 nM), 200 nM Cas12a and 400 nM crDNA. The Cas12a–crDNA complex was first prepared, incubated for 5 min at room temperature before being mixed with target RNA, incubated at 37 °C for 60 min then resolved by 5% native PAGE (37.5:1) at 4 °C (0.25× TBE buffer), 250 V for 12 min. RNA was visualized using a Bio-Rad gel imaging system.

RNA cleavage site mapping

A hydrolysis ladder (OH^-) was obtained by incubating 0.5 µl 100 µM 5′-FAM labeled target ssRNA in hydrolysis buffer at 95 °C for 30 min, before quenching on ice. The control ladder was a synthetic 5′-FAM-labeled 24-nt RNA fragment derived from target ssRNA.

The reaction was quenched by Inactivation/Precipitation Buffer (Thermo Fisher Scientific) and precipitation by microcentrifuge at 38,200*g* for 15 min at 4 °C before adding RNA gel-loading buffer (90% glycerol and 10% formamide). All products were resolved by 15% denaturing PAGE.

Electrophoretic mobility shift assays

Unless otherwise stated, to avoid dissociation of the Cas12a–crDNA or Cas12a–crRNA, complex at low concentrations during target ssRNA binding experiments, binding reactions contained a constant excess ratio of Cas protein and crDNA/crRNA/gRNA (2:1), and 50 nM of 5′-FAM-labeled target ssRNA. Reactions were incubated at 37 °C for 60 min before being resolved by 6% native PAGE (37.5:1) at 4 °C (0.25× TBE buffer), 120 V for 60 min. RNA and DNA were visualized by Bio-Rad gel imaging system.

For ternary complex analysis, binding reactions contained constant 5′-FAM-labeled target RNA (50 nM), then preparation of 200 nM Cas12a–crDNA, or Cas12a–crRNA complex (at a ratio of 2:1) and incubating for 30 min at room temperature, then gradient dilution to target concentration.

For binary complex analysis, binding reactions contained constant crDNA (50 nM), and increasing concentrations of Cas12a.

Trans-cleavage activity analysis

Unless otherwise stated, 5′-FAM- and 3′-BHQ1-labeled ssDNA probes were synthesized by GENEWIZ. For the general system, reactions were assembled with 50 nM Cas12a protein, 100 nM crDNA, 0.10 pM–20 nM activators and 500 nM probes in a total volume of 20 µl in PCR tube (Bio-Rad). The reaction was performed at 37 °C, with the buffer containing 10 mM Tris-HCl (pH 7.9), 50 mM NaCl, 10 mM $MgCl_2$ and 10 mg ml^{-1} bovine serum albumin (BSA). The fluorescent signal (485 nm excitation and 535 nm emission) was monitored with a qPCR system (Bio-Rad) with an interval time of 1 min.

Michaelis–Menten modeling

To measure the *trans*-cleavage kinetics of DNA-guided and RNA-guided Cas12a enzymes, we first prepared 1 µM solutions of the Cas12a–crDNA or Cas12–crRNA complex. This was achieved by incubating a mixture of 1 µM synthetic crDNA or crRNA with at least twofold excess of the corresponding Cas12a at 4 °C for 5 min on an ice plate. Cas12a–crDNA or Cas12–crRNA complexes were then activated for *trans*-cleavage activity by mixing and incubating these complexes with synthetic RNA or dsDNA at 100 nM concentration at 4 °C for 5 min on an ice plate and then incubating on a heating plate at 37 °C for 30 min. The latter step yielded a solution with an activated Cas12a concentration of 100 nM. We performed the *trans*-cleavage kinetics assay using 1 nM activated Cas12a and varied ssDNA reporter concentrations of 1,000; 2,000; 4,000; 8,000; 16,000 and 32,000 nM. Two replicates were taken for each concentration. The reaction velocities versus reporter concentration data were fitted to the Michaelis–Menten equation using GraphPad Prism v.10 to obtain the k_{cat}.

Limited proteolysis

Limited trypsin proteolysis assays were performed using 2.5 µg of purified AsCas12a in the absence or presence of crDNA at a 1:1.2 molar ratio. Protein samples were incubated with trypsin at a protease-to-substrate mass ratio of 1:100. Proteolysis reactions were carried out at 37 °C and quenched after 10 min by the addition of SDS–PAGE loading buffer. Reaction products were resolved by SDS–PAGE on precast 5% polyacrylamide gels and visualized by Coomassie staining using BeyoBlue Plus Coomassie Blue Super-Fast Staining Solution.

ssRNA, ssDNA or dsDNA target binding K_{d2} measurement using fluorescence polarization

Unless otherwise stated, FAM-labeled RNA or DNA oligonucleotides were procured from GENEWIZ. To prepare dsDNA substrates, the oligos were annealed at a concentration of 10 µM in an annealing buffer composed of 10 mM Tris-HCl (pH 7.5) and 100 mM NaCl. The solution was heated at 95 °C for 5 min and allowed to cool down gradually to room temperature. Once annealed, the dsDNA was diluted to a final concentration of 20 nM using a binding buffer containing 10 mM Tris-HCl (pH 7.9), 50 mM NaCl, and 10 mg ml^{-1} BSA.

To form the Cas DNP, or Cas RNP, Cas12a and its respective crDNA or crRNA were mixed at concentrations of 2 µM and 1 µM, respectively, in the binding buffer. This mixture was then incubated at room temperature (~25 °C) for 30 min. The DNP or RNP were subsequently serially diluted using the binding buffer. Equal volumes of the diluted DNP or RNP and target substrates were combined, resulting in a final concentration of 10 nM target. The reactions were incubated at room temperature for an additional 60 min. Fluorescence polarization reading of FAM fluorophore was then taken using the Molecular Devices FlexStation v.3 Multi-mode Microplate Reader (Thermo Fisher Scientific).

crDNA or crRNA binding K_{d1} measurement using fluorescence polarization

Unless otherwise stated, FAM-labeled crDNA or crRNA oligonucleotides were procured from GENEWIZ. Cas12a was serially diluted using the binding buffer containing 10 mM Tris-HCl (pH 7.9), 50 mM NaCl, and 10 mg ml^{-1} BSA. Equal volumes of the diluted Cas12a and crDNA or crRNA were combined, resulting in a final concentration of 10 nM guide nucleic acid. The reactions were allowed to incubate at room temperature for 60 min. Fluorescence polarization reading of FAM fluorophore was then taken using the Molecular Devices FlexStation 3 Multi-mode Microplate Reader (Thermo Fisher Scientific).

Recombinase polymerase amplification

In the RPA reaction, a 50 µl RPA reaction mixture contained 29.5 µl primer-free rehydration buffer, 1.2 µl forward primer (20 µM), 0.75 µl reverse primer (20 µM), 5 µl sample, 2.5 µl Mg acetate (280 mM) and 11.05 µl DNase/RNase-free water. The reaction was then incubated in 37 °C for 20 min.

In the RT–RPA reaction, a 50 µl RT–RPA reaction mixture contained 29.5 µl primer-free rehydration buffer, 1.2 µl forward primer (20 µM), 0.75 µl reverse primer (20 µM), 5 µl sample, 2.5 µl Mg acetate (280 mM), 1 µl Script IV RT (200 U μl^{-1}) and 10.05 µl DNase/RNase-free water.

SLEUTH detection

An optimized 20-µl DNA-guided CRISPR–Cas12a reaction was formulated, consisting of 50 nM Cas12a, 500 nM crDNA, 500 nM fluorescence reporter, 1× NEB r2.1 buffer and 2 µl of amplification solution placed on the lid. The amplification reaction also included 0.125 U μl^{-1} T7 RNA polymerase, 1× T7 RNA polymerase buffer, 0.25 mM rNTP, 0.48 µM primers and 1.6 µl of RPA or RT–RPA rehydration mixture (RPA kit from Amp-Future). The tube lid was incubated at 40 °C for 15 min to promote the production of RNA amplicons. Subsequently, 2 µl of the amplification solution was spun down and incubated at 37 °C for 30 min to allow the DNA-guided CRISPR–Cas12a reaction to proceed.

SARS-CoV-2 clinical sample collection

SARS-CoV-2 raw samples were obtained and inactivated in the Prince of Wales Hospital (Hong Kong). Clinical samples were pretreated for pure RNA collection using a TIANamp Virus DNA/RNA Kit (Tiangen; Beijing; China) and a fast column extraction kit within 20 mins.

SARS-CoV-2 detection with RT–qPCR

First, a 10 µl reaction mixture contained 0.1 µl Script IV reverse transcriptase enzyme, 0.5 µl reverse primer (10 µM), 1 µl dNTP mix (10 µM), 5 µl RNA template and 3.4 µl DEPC-treated H_2O was incubated for 10 mins at 50 °C. Notably, the RNA template-primer mix was preheated at 65 °C for 5 mins, and then incubated on ice for at least 1 min for annealing before reaction. Second, SARS-CoV-2 raw samples were validated with Takara Taq premix kit. In the qPCR reaction, a 25 µl reaction mixture contained 12.5 µl premix Taq, 0.5 µl forward primer (10 µM), 0.5 µl reverse primer (10 µM), 1 µl probe (10 µM), 2 µl cDNA template and 8.5 µl DEPC-treated H_2O. The qPCR program was 95 °C for 30 s, then 95 °C for 5 s, 60 °C for 20 s, 72 °C for 10 s for 40 cycles.

Analysis of SLEUTH fluorescence data

Each SLEUTH Cas12a cleavage reaction was added to a 100 µl tube and reacted in Bio-Rad PCR machine. Fluorescence measurements (FAM channel for SYBR Green based melting curve analysis or HEX channel for *trans*-cleavage signal) were then obtained every 60 s for a period of 1 h using the CFX Opus real-time PCR machine (Bio-Rad). The fluorescence signal datapoints were exported directly from the machine system that are background-subtracted signal treated signal. The s.e.m. (s.d.) of duplicates/triplicates are shown as error bars.

Plasmid construction

For mammalian expression, AsCas12a and mCherry were cloned into a pcDNA3.1 vector and linked by a P2A peptide to enable coexpression from a single transcript. EGFP was cloned separately into a pcDNA3.1 vector. Plasmid synthesis and assembly were carried out by GENEWIZ. Full construct sequences are provided in Supplementary Table 1.

RNA silencing reagent preparation

Complete Dulbecco's Modified Eagle Medium (DMEM) was prepared by combining 445 ml of basal DMEM with 50 ml of fetal bovine serum and 5 ml of penicillin–streptomycin in a sterile mixing vessel. The mixture was inverted gently until homogeneous, then stored at 2–8 °C for up to 3 months. To prepare 1× phosphate-buffered saline (PBS), 5 ml of 10× PBS stock solution was diluted with 45 ml of ultrapure water in a sterile container, mixed by gentle inversion and stored at room temperature for up to 6 months.

Cell culture

HEK293T cells were maintained in complete DMEM and passaged every 2–3 days at a 1:3 split ratio. Confluent cultures in 6 cm dishes (approximately 5×10^6 cells per dish) were monitored by phase-contrast microscopy for normal morphology and growth. For subculturing, approximately 30% of the total cell population (≈1.5×10^6 cells) was harvested by aspirating medium, trypsinizing for 2 min at 37 °C, and neutralizing with twice the volume of complete DMEM. Cells were collected by centrifugation at 90*g* for 3 min, the supernatant was removed, and the pellet resuspended gently in 1 ml of complete DMEM. The cell suspension was then transferred into a fresh 6 cm dish containing 5 ml of prewarmed medium and incubated at 37 °C with 5% CO_2.

Cell transfection

For EGFP reporter system, 1×10^5 cells per well were seeded in 48-well plates 24 h before transfection. Then, 200 ng of EGFP reporter plasmid, 400 ng of AsCas12a-mCherry or 0.3 µl of crDNA (100 µM) were mixed with 0.45 µl of Lipofectamine 3000, 0.6 µl P3000 (except crDNA) and 30 µl of Opti-MEM Reduced Serum Medium, respectively. Complexes were allowed to form for 15 min and then added dropwise to each well. Transfected cells were harvested 12 h post-transfection for flow cytometry, fluorescence microscopy observation and qPCR analysis.

For endogenous gene knockdown, 1×10^5 cells per well were seeded in 48-well plates 24 h before transfection. Then, 400 ng of AsCas12a-mCherry or 0.3 µl of crDNA (100 µM) were mixed with 0.45 µl of Lipofectamine 3000, 0.6 µl P3000 (except crDNA) and 30 µl of Opti-MEM Reduced Serum Medium, respectively. Complexes were allowed to form for 15 min and then added dropwise to each well. Transfected cells were harvested 12 h post-transfection for qPCR and transcriptome sequencing analysis.

Flow cytometry for quantification of EGFP expression

At 12 h after transfection as described above, cells were trypsinized with 1× Trypsin-EDTA. Then the cells were resuspended in cytometry buffer (0.6% BSA, 2 mM EDTA, 10 mM HEPES, pH 7.4 in 1× DPBS). Each sample was passed through a 35-µm cell strainer. Cells were then analyzed in a BD FACSDiscover S8 Cell Sorter. FCS files were then analyzed in FloJo v.10.10 to obtain the MFI of EGFP fluorescence in mCherry–cy5-positive cells.

RT–qPCR for relative quantification of mRNA

Total RNA was extracted from samples using the MolPure Flash Cell/Tissue Total RNA Kit (Yeasen Biotech) according to the manufacturer's instructions. Purified RNA was subsequently subjected to one-step RT–qPCR using the Hifair Advanced One Step RT–qPCR SYBR Green Kit. RT–qPCR was performed under the following cycling conditions: reverse transcription at 50 °C for 20 min, initial denaturation at 95 °C for 5 min, followed by 40 cycles of denaturation at 95 °C for 15 s and annealing/extension at 60 °C for 30 s. Fluorescence signals were acquired using a Bio-Rad real-time PCR system. Relative gene expression levels were quantified using the comparative Ct ($2^{-\Delta\Delta Ct}$) method, with the glyceraldehyde-3-phosphate dehydrogenase (*GAPDH*) gene serving as the internal reference transcript.

Structure prediction pipeline using AlphaFold3-guided molecular dynamic simulation

The initial crystal structures for *Acidaminococcus* sp. Cas12a (AsCas12a) were retrieved from the Protein Data Bank (PDB) under accession codes 4UN3 and 5B43, respectively.

To predict the 3D structure of our crDNA-guided RNA targeting tri-complex with cas12a, we used the following computational

workflow: first, the primary sequences of the target DNA, guide RNA and the cas12a protein were submitted to the AlphaFold server for structure prediction. The resulting protein–nucleic acid complex model was then optimized and prepared for molecular dynamics simulation using the CHARMM-GUI webserver, generating a GROMACS-compatible topology. The system underwent energy minimization followed by equilibration under constant number of particles, volume and temperature (NVT ensemble) and constant number of particles, pressure and temperature (NPT ensemble). Finally, a 300-ns molecular dynamics simulation was performed to allow structural relaxation and to refine the binding interactions within the predicted complex. Similar workflow was adopted for PAM-related mutation with AsCas12a as a binary complex prediction.

Cryo grid preparation and data collection

AsCas12a Ultra (6.4 µM) was incubated with crDNA (final 13 µM) and RNA (final 13 µM) in 10 mM Tris-HCl pH 8.0 and 50 mM NaCl at 37 °C for 30 min to form the ternary complex. Then, 4 µl of 2.5-fold diluted ternary complex was then applied to holey carbon grids (C-flat R1.2/1.3 Au, 300 mesh) after glow discharge (15 mA, 45 s). After incubation for 10 s at 4 °C and 100% humidity, the grids were blotted for 4 s with blotting paper, and then plunged quickly into liquid ethane cooled by liquid nitrogen with a Mark IV Vitrobot (Thermo Fisher Scientific). The grids were loaded into a FEI Titan Krios G3i electron microscope (Thermo Fisher Scientific) equipped with a high-brightness field emission gun operated at 300 kV. Images were collected automatically with a K3 Summit direct electron detector (Gatan) using EPU software (Thermo Fisher Scientific) in counting mode and magnification of ×81,000, corresponding to a 1.05 Å physical pixel size. The slit width of the Gatan Imaging Filter (GIF) Bio Quantum was set to 20 eV. The defocus ranges, dose rate and other parameters during image acquisition of the dataset are listed in Supplementary Table 4.

Drift correction and CTF correction were performed in CryoSPARC v.4.7.1[56]. Motion-corrected sums with dose-weighting were used for all subsequent image processing. Blob picking on 500 micrographs was first used to obtain the initial particle stack. After cleaning with two-dimensional classification and heterogenous refinement, the particles of classes with clear AsCas12a features were used as templates to pick on the full 2,030 micrographs. Two rounds of heterogenous refinements were then used to obtain a clean stack of 1,305,848 particles, which showed preferred orientation. Rebalance orientations in CryoSPARC v.4.7.1[57] was used twice to remove excessive side views, resulting in 277,781 particles as the final stack to reconstruct the consensuses map for subsequent 3D classifications in CryoSPARC v.4.7.1[56] and Relion v.5[57]. The data processing flowchart is shown in Supplementary Fig. 9.

Model building

Models of PDB 8SFL were first docked into the final map using fit in map function of ChimeraX v.1.9[58]. The models of bound crDNA and RNA were then fitted into the density, matching the distinct purine/pyrimidine patterns and their known sequences. Coot v.0.9.8.96[59] was used to adjust the model manually. The model was refined against the corresponding cryo-EM density map with phenix.real_space_refine module in PHENIX v.1.21.2-5419 package[60]. The qualities of the final refined model were estimated with MolProbity[61]. The figures on maps and refined models were generated with ChimeraX v.1.9. Refinement statistics are presented in Supplementary Table 4.

Reporting summary

Further information on research design is available in the Nature Portfolio Reporting Summary linked to this article.

Data availability

All nucleic acid sequences used in this study are provided in the paper or Supplementary Information. The model and maps of AsCas12a in complex with crDNA and target RNA are deposited with PDB 22FN and EMD-68245, respectively. The structural models generated in this study using AlphaFold3-guided molecular dynamic simulation are available via Zenodo at https://doi.org/10.5281/zenodo.19103630 (ref. 62). Raw RNA-seq data generated in this study have been deposited in the NCBI Sequence Read Archive under BioProject accession PRJNA1439200. All raw data supporting the findings of this study are available in publicly accessible repositories or in the Supplementary Information.

References

56. Punjani, A., Rubinstein, J. L., Fleet, D. J. & Brubaker, M. A. cryoSPARC: algorithms for rapid unsupervised cryo-EM structure determination. *Nat. Methods* **14**, 290–296 (2017).
57. Scheres, S. H. W. RELION: Implementation of a Bayesian approach to cryo-EM structure determination. *J. Struct. Biol.* **180**, 519–530 (2012).
58. Meng, E. C. et al. UCSF ChimeraX: tools for structure building and analysis. *Protein Sci.* **32**, e4792 (2023).
59. Emsley, P., Lohkamp, B., Scott, W. G. & Cowtan, K. Features and development of Coot. *Acta Crystallogr. D* **66**, 486–501 (2010).
60. Adams, P. D. et al. PHENIX: a comprehensive Python-based system for macromolecular structure solution. *Acta Crystallogr. D* **66**, 213–221 (2010).
61. Chen, V. B. et al. MolProbity: all-atom structure validation for macromolecular crystallography. *Acta Crystallogr. D* **66**, 12–21 (2010).
62. Wu, X. Cas12a-crDNA-RNA target structure prediction using AlphaFold3 guided molecular dynamic simulation. *Zenodo* https://doi.org/10.5281/zenodo.19103630 (2026).

Acknowledgements

Clinical samples were provided by The Prince of Wales Hospital with approval from the Chinese University of Hong Kong Clinical Research Ethics Committee (CREC-2021-0188). We thank G. C. Y. Lui, S. S. Lee and D. P. C. Chan for assistance with clinical sample collection. We thank the Biosciences Central Research facility, HKUST (Clear Water Bay) for providing instruments and services. We thank the developers of OpenAI's ChatGPT for assistance with language editing of the paper. Funding was provided in part by the Research Grants Council (6107-20G, 16303522, 16304225 to I.-M.H. and C6053-25G, C7035-23GF to Y.Z.) of the Hong Kong SAR Government, China and by the National Natural Science Foundation of China (325014 to Y.Z.). We also thank the Biological Cryo-EM Center at the Hong Kong University of Science and Technology (HKUST) for sample screening, grids preparation and data collection. The HKUST Cryo-EM Center is generously supported by a donation from the Lo Kwee Seong Foundation.

Author contributions

Conceptualization: I.-M.H. and X.W. Methodology: I.-M.H., X.W., Y.C., Z.Z., W.H.L. and Y.Z. Software: Z.Z. Validation: X.W., Y.C. and Z.Z. Formal analysis: X.W., Y.C., Z.Z., H.L., X.F. and W.H.L. Investigation: X.W., Y.C., Z.Z., H.L. and X.F. Resources: I.-M.H. and Y.Z. Data curation: X.W., Y.C., Z.Z., H.L. and W.H.L. Visualization: X.W., Y.C., Z.Z. and W.H.L. Funding acquisition: I.-M.H. Project administration: I.-M.H. Supervision: I.-M.H. Writing—original draft: X.W., H.L., Y.C., Z.Z. and X.F. Writing—review and editing: I.-M.H., X.W., H.L., Z.Z., X.F., W.H.L. and Y.Z.

Competing interests

I.-M.H. and X.W. are co-inventors on a US provisional patent application (US 63/798595), entitled Methods and Components for DNA-guided RNA Targeting CRISPR–Cas Systems, related to this work and filed by The Hong Kong University of Science and Technology. The other authors declare no competing interests.

Additional information

Supplementary information The online version contains supplementary material available at https://doi.org/10.1038/s41587-026-03120-5.

Correspondence and requests for materials should be addressed to I-Ming Hsing.

Peer review information *Nature Biotechnology* thanks Chase Beisel and the other, anonymous, reviewer(s) for their contribution to the peer review of this work. Peer reviewer reports are available.

Reprints and permissions information is available at www.nature.com/reprints.

nature portfolio

Corresponding author(s): I-ming Hsing

Last updated by author(s): Mar 24, 2026

Reporting Summary

Nature Portfolio wishes to improve the reproducibility of the work that we publish. This form provides structure for consistency and transparency in reporting. For further information on Nature Portfolio policies, see our Editorial Policies and the Editorial Policy Checklist.

Statistics

For all statistical analyses, confirm that the following items are present in the figure legend, table legend, main text, or Methods section.

n/a	Confirmed
☐	☒ The exact sample size (*n*) for each experimental group/condition, given as a discrete number and unit of measurement
☐	☒ A statement on whether measurements were taken from distinct samples or whether the same sample was measured repeatedly
☐	☒ The statistical test(s) used AND whether they are one- or two-sided *Only common tests should be described solely by name; describe more complex techniques in the Methods section.*
☒	☐ A description of all covariates tested
☒	☐ A description of any assumptions or corrections, such as tests of normality and adjustment for multiple comparisons
☐	☒ A full description of the statistical parameters including central tendency (e.g. means) or other basic estimates (e.g. regression coefficient) AND variation (e.g. standard deviation) or associated estimates of uncertainty (e.g. confidence intervals)
☐	☒ For null hypothesis testing, the test statistic (e.g. *F*, *t*, *r*) with confidence intervals, effect sizes, degrees of freedom and *P* value noted *Give P values as exact values whenever suitable.*
☒	☐ For Bayesian analysis, information on the choice of priors and Markov chain Monte Carlo settings
☒	☐ For hierarchical and complex designs, identification of the appropriate level for tests and full reporting of outcomes
☒	☐ Estimates of effect sizes (e.g. Cohen's *d*, Pearson's *r*), indicating how they were calculated

Our web collection on statistics for biologists contains articles on many of the points above.

Software and code

Policy information about availability of computer code

Data collection	The fluorescence signal intensities in this study was determined and collected by using CFX Opus 96 Real-Time PCR machine (Bio-Rad). The gels were visualized by GelDoc Go imaging system (Bio-Rad). Fluorescence polarization data was collected using the Molecular Devices FlexStation 3 Multi-mode Microplate Reader (Thermo Fisher Scientific). Fluorescence images were captured by a fluorescence microscope (Chinetek Scientific). Structure prediction was performed in AlphaFold 3 server. The resulting protein-nucleic acid complex model was then optimized and prepared for molecular dynamics (MD) simulation using the CHARMM-GUI webserver, generating a GROMACS-compatible topology. Cryo-EM Images were automatically collected with a K3 Summit direct electron detector (Gatan) using EPU software (Thermo Fisher Scientific) in counting mode.
Data analysis	Fluorescence signal and qPCR data were analyzed using Bio-Rad CFX Maestro. Statistical analysis was performed with Origin Lab version 2024b or GraghPad Prism 10. Fluorescence images intensity were processed with Image J. Fluorescence polarization data was analyzed by SoftMax Pro 7.0.3. Simulation results were analyzed and visualized by ChimeraX v1.9. The cutoff values were determined by computing the negative samples and subsequently adding three times the standard deviation. RNA sequencing data was analyzed by GENEWIZ. Cryo-EM data were processed in CryoSPARC v4.7.1 for drift and CTF correction. Initial models were docked into the final maps in ChimeraX v1.9, manually adjusted in Coot 0.9.8.96, and refined against the cryo-EM density maps using phenix.real_space_refine in PHENIX 1.21.2-5419. Model quality was assessed with MolProbity. Figures were prepared in ChimeraX v1.9.

For manuscripts utilizing custom algorithms or software that are central to the research but not yet described in published literature, software must be made available to editors and reviewers. We strongly encourage code deposition in a community repository (e.g. GitHub). See the Nature Portfolio guidelines for submitting code & software for further information.

Data

Policy information about availability of data

All manuscripts must include a data availability statement. This statement should provide the following information, where applicable:

- Accession codes, unique identifiers, or web links for publicly available datasets
- A description of any restrictions on data availability
- For clinical datasets or third party data, please ensure that the statement adheres to our policy

All nucleic acid sequences used in this study are provided in manuscripts or supplementary information. The model and maps of AsCas12a in complex with crDNA and target RNA are deposited to PDB and EMDB with codes 22FN and EMD-68245, respectively. The structural models generated in this study using AlphaFold3 guided molecular dynamic simulation are available at Zenodo under DOI [10.5281/zenodo.19103630]. Raw RNA-seq data generated in this study have been deposited in the NCBI Sequence Read Archive under BioProject accession [PRJNA1439200]. Source data are provided with this paper. All other raw data supporting the findings of this study are available in publicly accessible repositories or in the Supplementary Information.

Research involving human participants, their data, or biological material

Policy information about studies with human participants or human data. See also policy information about sex, gender (identity/presentation), and sexual orientation and race, ethnicity and racism.

Reporting on sex and gender	SARS-CoV-2 swab samples used in this study were obtained from the Prince of Wales Hospital under approval from the Clinical Research Ethics Committee of The Chinese University of Hong Kong (CREC-2021-0188). Samples were selected based on availability. Age and sex were not used as variables in sample selection or analysis, and individual-level demographic information was not available to the investigators.
Reporting on race, ethnicity, or other socially relevant groupings	Race, ethnicity and other socially relevant groupings were not collected or used in this study. The clinical swab samples were obtained from the Prince of Wales Hospital.
Population characteristics	SARS-CoV-2 swab samples used in this study were obtained from the Prince of Wales Hospital under approval from the Clinical Research Ethics Committee of The Chinese University of Hong Kong (CREC-2021-0188). Samples were selected based on availability. Age and sex were not used as variables in sample selection or analysis, and individual-level demographic information was not available to the investigators. Based on qPCR results, 30 samples were positive for SARS-CoV-2 and 1 sample was negative.
Recruitment	SARS-CoV-2 clinical samples were provided by The Prince of Wales Hospital with approval from the Chinese University of Hong Kong Clinical Research Ethics Committee (CREC-2021-0188).
Ethics oversight	SARS-CoV-2 clinical samples were provided by The Prince of Wales Hospital with approval from the Chinese University of Hong Kong Clinical Research Ethics Committee (CREC-2021-0188).

Note that full information on the approval of the study protocol must also be provided in the manuscript.

Field-specific reporting

Please select the one below that is the best fit for your research. If you are not sure, read the appropriate sections before making your selection.

☒ Life sciences ☐ Behavioural & social sciences ☐ Ecological, evolutionary & environmental sciences

For a reference copy of the document with all sections, see nature.com/documents/nr-reporting-summary-flat.pdf

Life sciences study design

All studies must disclose on these points even when the disclosure is negative.

Sample size	No statistical method was used to predetermine sample size. Sample sizes were chosen based on standard practice, sample availability and feasibility. Exact n values and whether replicates were technical or biological are provided in the figure legends.
Data exclusions	No data were excluded from the analyses.
Replication	Each experiment was done with at least 2 replicates to ensure that the results are reproducible. All attempts at replication were successful, and standard deviations were within the expected ranges.
Randomization	Randomization was not relevant to most in vitro biochemical experiments.
Blinding	Blinding was not performed, because the primary readouts were instrument-based quantitative measurements (fluorescence, RT-qPCR and flow cytometry) analyzed using predefined criteria.

Reporting for specific materials, systems and methods

We require information from authors about some types of materials, experimental systems and methods used in many studies. Here, indicate whether each material, system or method listed is relevant to your study. If you are not sure if a list item applies to your research, read the appropriate section before selecting a response.

Materials & experimental systems

n/a	Involved in the study
☒	☐ Antibodies
☐	☒ Eukaryotic cell lines
☒	☐ Palaeontology and archaeology
☒	☐ Animals and other organisms
☒	☐ Clinical data
☒	☐ Dual use research of concern
☒	☐ Plants

Methods

n/a	Involved in the study
☒	☐ ChIP-seq
☐	☒ Flow cytometry
☒	☐ MRI-based neuroimaging

Eukaryotic cell lines

Policy information about cell lines and Sex and Gender in Research

Cell line source(s)	HEK293T (IM-H222) was from Xiamen Immocell Biotechnology Co.,Ltd. (Xiamen)
Authentication	All cell lines obtained from Xiamen Immocell Biotechnology Co.,Ltd. were authenticated by the provider.
Mycoplasma contamination	All cell lines were routinely tested for mycoplasma contamination using PCR-based detection, and all tested negative prior to experiments.
Commonly misidentified lines (See ICLAC register)	HEK293T is not listed as a commonly misidentified cell line in the ICLAC register.

Plants

Seed stocks	*Report on the source of all seed stocks or other plant material used. If applicable, state the seed stock centre and catalogue number. If plant specimens were collected from the field, describe the collection location, date and sampling procedures.*
Novel plant genotypes	*Describe the methods by which all novel plant genotypes were produced. This includes those generated by transgenic approaches, gene editing, chemical/radiation-based mutagenesis and hybridization. For transgenic lines, describe the transformation method, the number of independent lines analyzed and the generation upon which experiments were performed. For gene-edited lines, describe the editor used, the endogenous sequence targeted for editing, the targeting guide RNA sequence (if applicable) and how the editor was applied.*
Authentication	*Describe any authentication procedures for each seed stock used or novel genotype generated. Describe any experiments used to assess the effect of a mutation and, where applicable, how potential secondary effects (e.g. second site T-DNA insertions, mosiacism, off-target gene editing) were examined.*

Flow Cytometry

Plots

Confirm that:

☐ The axis labels state the marker and fluorochrome used (e.g. CD4-FITC).

☐ The axis scales are clearly visible. Include numbers along axes only for bottom left plot of group (a 'group' is an analysis of identical markers).

☐ All plots are contour plots with outliers or pseudocolor plots.

☒ A numerical value for number of cells or percentage (with statistics) is provided.

Methodology

Sample preparation	Cells were collected and washed with PBS, prepared as single-cell suspensions with cytometry buffer (0.6% BSA, 2mM EDTA, 10mM HEPES, pH=7.4 in 1X DPBS).
Instrument	BD FACSDiscover™ S8 Cell Sorter
Software	FloJoTM v.10.10

Cell population abundance	The analyzed cell populations were readily detectable in all samples and sufficient for quantitative analysis.
Gating strategy	Cells were first gated on FSC-A versus SSC-A to exclude debris, followed by FSC-H versus FSC-A gating to select singlets. Healthy cells were then selected based on FSC-A versus Light Loss-A. Final analysis was performed using YG3 (mCherry) and YG6 (Cy5) fluorescence. For Cas12a + crDNA co-transfection experiments, YG3/YG6 double-positive cells were analyzed; for crDNA-only experiments, YG6-positive cells were analyzed.

☐ Tick this box to confirm that a figure exemplifying the gating strategy is provided in the Supplementary Information.